

# The Carnegie-Irvine Galaxy Survey. IX. Classification of Bulge Types and Statistical Properties of Pseudo Bulges

HUA GAO (高桦)<sup>1,2</sup> LUIS C. HO,<sup>2,1</sup> AARON J. BARTH,<sup>3</sup> AND ZHAO-YU LI<sup>4</sup>

<sup>1</sup>*Department of Astronomy, School of Physics, Peking University, Beijing 100871, China*

<sup>2</sup>*Kawli Institute for Astronomy and Astrophysics, Peking University, Beijing 100871, China*

<sup>3</sup>*Department of Physics and Astronomy, University of California at Irvine, 4129 Frederick Reines Hall, Irvine, CA 92697-4575, USA*

<sup>4</sup>*Department of Astronomy, Shanghai Jiao Tong University, Shanghai 200240, China*

## ABSTRACT

We study the statistical properties of 320 bulges of disk galaxies in the Carnegie-Irvine Galaxy Survey, using robust structural parameters of galaxies derived from image fitting. We apply the Kormendy relation to classify classical and pseudo bulges and characterize bulge dichotomy with respect to bulge structural properties and physical properties of host galaxies. We confirm previous findings that pseudo bulges on average have smaller Sérsic indices, smaller bulge-to-total ratios, and fainter surface brightnesses when compared with classical bulges. Our sizable sample statistically shows that pseudo bulges are more intrinsically flattened than classical bulges. Pseudo bulges are most frequent (incidence  $\gtrsim 80\%$ ) in late-type spirals (later than Sc). Our measurements support the picture in which pseudo bulges arose from star formation induced by inflowing gas, while classical bulges were born out of violent processes such as mergers and coalescence of clumps. We reveal differences with the literature that warrant attention: (1) the bimodal distribution of Sérsic indices presented by previous studies is not reproduced in our study; (2) classical and pseudo bulges have similar relative bulge sizes; and (3) the pseudo bulge fraction is considerably smaller in early-type disks compared with previous studies based on one-dimensional surface brightness profile fitting. We attribute the above differences to our improved image quality, more robust bulge-to-disk decomposition technique, and different classification criteria applied. Moreover, we find that barred galaxies do not host more pseudo bulges or more prominent pseudo bulges than unbarred galaxies. Various implications of these findings are discussed.

*Keywords:* Galaxy bulges (578), Galaxy structure (622), Galaxy photometry (611), Disk galaxies (391), Elliptical galaxies (456), Galaxy evolution (594)

## 1. INTRODUCTION

The fundamental plane of elliptical galaxies was first established in the 1980s (Djorgovski & Davis 1987; Dressler et al. 1987) and has long proved to be a useful tool to estimate distances and to study the formation and evolution of these systems (Dressler et al. 1987; Faber et al. 1987; Djorgovski et al. 1988; Lynden-Bell et al. 1988; D’Onofrio et al. 2013, 2017; Zhang & Zaritsky 2016). The fundamental plane is a three-parameter correlation of the galaxy half-light (effective) radius  $r_e$ , central velocity dispersion  $\sigma_0$ , and average effective surface brightness  $\langle\mu_e\rangle$ :

$$\log r_e = a \log \sigma_0 + b \langle\mu_e\rangle + c. \quad (1)$$

At the most basic level, the physical root of the relation is the virial theorem (Djorgovski & Davis 1987; Djorgovski et al. 1988; Kormendy & Djorgovski 1989),

$$\frac{GM}{r_g} \sim \langle v^2 \rangle, \quad (2)$$

where  $M$  is the total mass,  $r_g$  is the gravitational radius, and  $\langle v^2 \rangle$  is the mean square of stellar velocity (Binney & Tremaine 2008). To translate the physical parameters in the virial theorem into observables, one has to make assumptions of the density, kinematic structure, and dynamical mass-to-light ratio ( $M/L$ ) of the galaxies. Rewriting Equation 2 to follow the formulation of Equation 1, we have

$$\log r_e = 2 \log \sigma_0 + 0.4 \langle\mu_e\rangle + \log \left[ k \left( \frac{M}{L} \right)^{-1} \right] + C, \quad (3)$$

where  $k$  accounts for the projection effect and intrinsic density and kinematic structure of the galaxies. The observed coefficients  $a$  and  $b$  in Equation 1 generally deviate from 2 and 0.4, respectively, which is commonly termed the tilt of the fundamental plane with respect to the virial plane. The heterogeneity of density and kinematic structures and dynamical mass-to-light ratios of ellipticals may contribute to the tilt, although which factor plays a dominant role is still debated. Ellipticals have long been approximated as homologous stellar systems, so the contribution of heterogeneity of their structures to the tilt was often neglected. Assuming that ellipticals have homologous density and kinematics, some authors found  $M/L \sim M^{0.2}$  (Djorgovski 1987; Faber et al. 1987; Pahre et al. 1998; Treu et al. 2005). Factors that may lead to variations of dynamical mass-to-light ratio include metallicity (e.g., Djorgovski & Davis 1987), initial mass function (e.g., Kroupa 2001; Renzini & Ciotti 1993; Cappellari et al. 2012), and dark matter (e.g., Ciotti et al. 1996; Cappellari et al. 2006, 2013a). In addition to the aforementioned possibilities, the heterogeneity of density and kinematics of ellipticals may also tilt the fundamental plane. Ellipticals are now known to be not strictly homologous in terms of light profile (Nieto et al. 1991; Lauer et al. 1995, 2005, 2007; Kormendy et al. 1996, 2009; Bertin et al. 2002) and kinematic structure (Illingworth 1977; Davies et al. 1983; Bender 1987, 1988; Emsellem et al. 2011). Busarello et al. (1997) stressed the importance of kinematic heterogeneity in causing the tilt, and that structural heterogeneity and stellar population effects play a minor role. On the contrary, D’Onofrio et al. (2013) concluded that the tilt is mainly affected by structural heterogeneity. However, Ciotti et al. (1996) and Cappellari et al. (2006, 2013a) disagree. Apart from the tilt, studying the residuals of the fundamental plane provides insights into and constrains the regularity/stochasticity of the formation and evolution of elliptical galaxies (Renzini & Ciotti 1993; Borriello et al. 2003; D’Onofrio et al. 2013, 2017).

Even though ellipticals are not a strictly homologous population, the tightness of the fundamental plane implies their highly regulated formation and evolution pathways, especially when compared with other stellar systems. For example, star-forming disks on the other end of the Hubble sequence differ from the ellipticals in every aforementioned aspect that could cause the tilt and amplify the scatter of the scaling relations. Hence, the fundamental plane relation is useful to distinguish stellar systems of distinct physical nature. One notably successful example in application of the fundamental plane projections and their variants was the discovery of the dichotomy between elliptical and spheroidal galax-

ies (Kormendy 1985, 1987; Bender et al. 1992; Binggeli 1994). These authors showed that spheroidal galaxies form a sequence distinct from that of ellipticals in the core parameter correlations (i.e., central surface brightness and core radius—a projection of the core fundamental plane; see Lauer 1985; Kormendy 1985, 1987; Binggeli 1994) and in the  $\kappa$  formulation of the fundamental plane (Bender et al. 1992). Surprisingly, in these parameter spaces spheroidals occupy a locus that overlaps with the disks of spiral galaxies. The dichotomy between slow-rotator and fast-rotator ellipticals (e.g., Illingworth 1977; Davies et al. 1983; Emsellem et al. 2011) is also another manifestation of the application of the core parameter correlations, but it is much less obvious than the elliptical vs. spheroidal dichotomy (Faber et al. 1997).

Since the seminal work of van den Bergh (1976), Combes & Sanders (1981), Gallagher et al. (1982), Kormendy (1982a,b, 1993), Kormendy & Illingworth (1982, 1983), Pfenniger (1984, 1985), Combes et al. (1990), and Pfenniger & Norman (1990), two classes of bulges are recognized in disk (S0 and spiral) galaxies. Classical bulges have similar observational properties as ellipticals (Faber 1977; Gott 1977; Renzini 1999) and are therefore considered to form out of rapid, violent processes such as mergers and coalescence of clumps (Toomre 1977; Bournaud 2016). They follow the scaling relations defined by ellipticals (Kormendy 1985, 1987; Bender et al. 1992). On the other hand, pseudo bulges are more likely central miniature disks embedded in the large-scale disks. They have younger, more composite stellar populations, more flattened stellar light distribution, and more rotation-dominated kinematics compared with classical bulges (e.g., Wyse et al. 1997; Kormendy & Kennicutt 2004; Fisher & Drory 2016; Kormendy 2016). In contrast with the violent origin of classical bulges, pseudo bulges are deemed to form out of redistributed disk material by gradual, secular processes facilitated by non-axisymmetry in the galaxy potential (Combes & Sanders 1981; Kormendy 1981, 1982b; Pfenniger & Norman 1990; Sellwood & Wilkinson 1993). Pseudo bulges are found to be low-surface brightness outliers in the Kormendy (1977) relation—the correlation between surface brightness and effective radius of ellipticals, which constitutes the photometric projection of the fundamental plane (e.g., Carollo 1999; Gadotti 2009; Fisher & Drory 2010; Laurikainen et al. 2010; but see Kim et al. 2017; Kim & Ho 2019; Zhao et al. 2019 for the case of active galaxies). The dichotomy between classical and pseudo bulges is the main subject of this paper.

In addition to using the Kormendy relation, there are alternative ways to distinguish classical bulges from

pseudo bulges. For example, the Sérsic (1968) index  $n$  is widely used to separate the two categories of bulges. Based on the bimodal distribution of  $n$  found by Fisher & Drory (2008, 2016), these authors proposed that pseudo bulges be defined by  $n < 2$ . Bulge type is statistically linked with Hubble type (pseudo bulges occur most frequently in spirals of type Sbc and later; Kormendy & Kennicutt 2004, and references therein), and thus bulge-to-total ratio ( $B/T$ ), but the correspondence is imperfect because the correlation between Hubble type and  $B/T$  has large scatter (e.g., Kent 1985; Simien & de Vaucouleurs 1986; de Jong 1996; Grosbøl et al. 2004; Laurikainen et al. 2007, 2010; Weinzirl et al. 2009; Méndez-Abreu et al. 2017; Gao et al. 2019). While a low  $B/T$  does not guarantee a pseudo bulge, pseudo bulges are generally found in galaxies with  $B/T \lesssim 0.35$ ; if  $B/T \gtrsim 0.5$ , the bulge is very likely classical (Kormendy & Ho 2013; Kormendy 2016). Bulge size was used in conjunction with  $B/T$  to classify bulges in Allen et al. (2006). Central morphological features, such as nuclear bars/rings/spirals that are indicative of kinematically cold bulges, boxy/peanut bulges that are actually thickened bars, or apparent flattenings similar to those of disks, are useful diagnostics to recognize pseudo bulges (e.g., Kormendy & Kennicutt 2004; Fisher & Drory 2008, 2010; Fisher et al. 2009; Kormendy & Ho 2013; Kormendy 2016). Stellar kinematics provide perhaps the cleanest diagnostic, but they are not readily available for large samples. Pseudo bulges are characterized by their larger degree of rotation relative to random motion (Kormendy & Illingworth 1982; Kormendy 1982a), stand out as low- $\sigma$  outliers in the Faber-Jackson (1976) relation (Kormendy & Illingworth 1983; Kormendy & Kennicutt 2004), and have flat central  $\sigma$  profiles (Fisher & Drory 2016). Some extreme cases even show “ $\sigma$  drops” at the center. Vigorous star formation and young stellar populations, if not induced by mergers, are signposts of on-going growth of pseudo bulges (Kormendy & Kennicutt 2004; Fisher et al. 2009; Fisher & Drory 2016). For complete reviews of the observational criteria to classify classical and pseudo bulges, see Kormendy & Kennicutt (2004), supplemental material of Kormendy & Ho (2013), Fisher & Drory (2016), and Kormendy (2016). Unfortunately, these many criteria do not necessarily produce consistent results. Robust classifications can be achieved by applying as many criteria as possible. To resolve the ambiguity, Neumann et al. (2017) performed a comprehensive comparison among the commonly adopted criteria: Sérsic index, concentration index, the Kormendy relation, and the inner slope of radial velocity dispersion profile. They found that the Kormendy relation is the best single criterion, as it is

able to recover 39 out of 40 “safe” classifications, where safe classifications were defined as consistent classifications resulted from at least three out of the four criteria.

In order to characterize bulge dichotomy in the local Universe, we will consistently apply the Kormendy relation to classify classical and pseudo bulges, as it has a strong physical basis and provides the best agreement with classifications based on multiple criteria. We do not consider the full fundamental plane because stellar central velocity dispersions are not available for a significant fraction of the spiral galaxies in our sample. We will use the robust structural parameters derived in Gao et al. (2019). The rest of this paper will be devoted to introduction of the Carnegie-Irvine Galaxy Survey (CGS; Ho et al. 2011), measuring the Kormendy relation of CGS ellipticals and bulges, classifying classical and pseudo bulges, studying their statistical properties, and discussing implications on their respective formation and evolution paths.

## 2. SAMPLE AND DATA

The CGS sample is defined by  $B_T \leq 12.9$  mag and  $\delta < 0^\circ$ , without any reference to morphology, size, or environment. Details of the observations and data reduction are given in Ho et al. (2011) and Li et al. (2011), and will not be repeated here. In this study, we mainly use products from the  $R$ -band images. The majority of the images are of high quality, in terms of field-of-view ( $8'.9 \times 8'.9$ ), median seeing ( $1''.01$ ), and median surface brightness depth ( $26.4$  mag arcsec $^{-2}$ ).

In this paper, we make use of all the successfully decomposed disk galaxies presented in Gao et al. (2019). The CGS disk galaxy sample for bulge-to-disk decomposition is restricted to the subset of galaxies with morphological type index  $-3 \leq T \leq 9.5$  and inclination angle  $i \leq 70^\circ$ . After complementing the sample with a handful of misclassified ellipticals and removing objects whose decomposition was unsuccessful, the final sample consists of 320 S0s and spirals. Basic properties of the sample are discussed in detail in Gao et al. (2019) and will not be repeated here. Below we briefly describe the decomposition strategy; we refer readers to Section 3 of Gao et al. (2019) for full details of the decomposition. We performed multi-component decomposition of the  $R$ -band images to derive accurate bulge structural parameters, following closely the technique described in Gao & Ho (2017) and Gao et al. (2018). In addition to bulges and disks, we successfully modeled nuclei, bars, disk breaks, nuclear/inner lenses, and inner rings. Our modeling strategy treats nuclear rings and nuclear bars as part of the bulge component, while other features such as spiral arms, outer lenses, and outer rings were

omitted from the fits because they are not crucial for accurate bulge measurements according to the experiments in Gao & Ho (2017). The error budget of the bulge parameters includes the uncertainties from sky level measurements and model assumptions.

In addition to the disk galaxy sample, we perform single-Sérsic fits to 83 ellipticals to measure their structural parameters in the  $R$  band (Appendix A). The CGS elliptical sample is drawn from Huang et al. (2013a). We remove misclassified ellipticals that have since been classified as S0s in Gao et al. (2018). Although Huang et al. (2013a) promoted the three-component nature of ellipticals, single-Sérsic fits suffice for our purpose of deriving global structural parameters for reference comparison with the bulges on the fundamental plane correlations. The uncertainties of the structural parameters stem from the uncertainties in sky subtraction. We estimate the uncertainties in a manner consistent with the bulge measurements. Namely, we measure the sky-induced uncertainties as variations of the best-fit parameters when perturbing the sky levels around  $\pm 1\sigma_{\text{sky}}$  of the measured sky levels, where uncertainties of the sky level  $\sigma_{\text{sky}}$  are measured as the root-mean-square of the residuals determined from randomly placed boxes in the sky-dominated region of the sky-subtracted data image (see Appendix B of Gao & Ho 2017 for details). Considering that ellipticals are more extended than disk galaxies and a single Sérsic function cannot accurately describe their light profiles across a large dynamical range in radius, we strive to avoid introducing model-induced uncertainties to sky level measurements, which in return may induce errors in Sérsic index measurements. Therefore, instead of simultaneously fitting the sky with the galaxy, as was done for the disk galaxies, we measure the sky level using the direct approach described in Gao & Ho (2017; their Appendix B.1) and subtract it before performing the fits.

### 3. RESULTS

#### 3.1. The Kormendy Relation of Ellipticals

We derive the Kormendy relation of the ellipticals by minimizing the  $\chi^2$ , defined as,

$$\chi^2 = \sum_{i=1}^N \frac{(\langle \mu_{e,i} \rangle - \alpha \log r_{e,i} - \beta)^2}{\xi_{\langle \mu_{e,i} \rangle}^2 + \alpha^2 \xi_{\log r_{e,i}}^2}, \quad (4)$$

where  $\alpha$  and  $\beta$  are the coefficients of the Kormendy relation  $\langle \mu_e \rangle = \alpha \log r_e + \beta$  and  $\xi$  denotes the uncertainties. The best-fit relation is

$$\langle \mu_e \rangle = (2.38 \pm 0.07) \log r_e + (17.86 \pm 0.04), \quad (5)$$

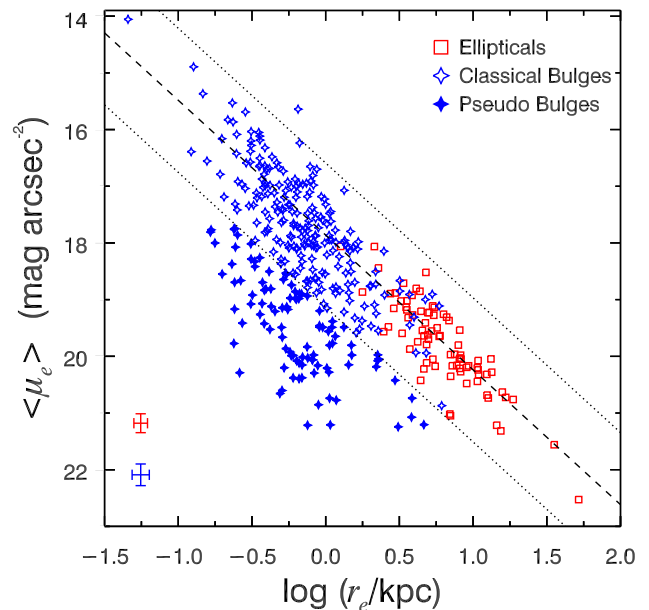


**Figure 1.** The Kormendy relation of CGS ellipticals and bulges. The best-fit relation and its  $3\sigma$  boundary of the ellipticals are indicated by the short-dashed lines and dotted lines, respectively. Typical uncertainties are illustrated in the bottom-left corner. Blue filled stars represent pseudo bulges that are  $3\sigma$  outliers from the best-fit relation of the ellipticals (red squares). The other bulges (blue open stars) are designated as classical bulges.

with a scatter of 0.42 dex in  $\langle \mu_e \rangle$ . We correct  $\langle \mu_e \rangle$  for Galactic extinction, following Ho et al. (2011) and Li et al. (2011).

The best-fit relation is shown in Figure 1, with the bulges of the disk galaxies overlaid. It is immediately apparent that some of the bulges overlap with and continuously extend the high- $\langle \mu_e \rangle$ , low- $r_e$  end of the Kormendy relation (the open blue stars), while others (the filled stars) scatter to low values of  $\langle \mu_e \rangle$  at fixed  $r_e$ . We classify as pseudo bulges those that scatter more than  $3\sigma$  below the best-fit Kormendy relation of ellipticals and the rest as classical bulges. Namely, pseudo bulges satisfy

$$\langle \mu_e \rangle > 2.38 \log r_e + 19.12, \quad (6)$$

where  $\langle \mu_e \rangle$  and  $r_e$  are measured in the  $R$  band and  $r_e$  is in units of kpc. This relation can be translated to other photometric bands using standard colors of ellipticals from Fukugita et al. (1995). This yields 101 pseudo bulges. Interestingly, only one of the pseudo bulges resides in an S0 galaxy—NGC 4802. Its bulge is dusty but overall blue, signaling recent star formation.

#### 3.2. Classical Bulges Are Not Necessarily Prominent

Figure 2 shows the distribution of  $B/T$  in the Kormendy relation (panel b). To mitigate the effects of

object overlay, we present a version smoothed by locally weighted regression (LOESS; Cleveland & Devlin 1988)<sup>1</sup> to highlight the general trend (panel c). We find that bulges with constant  $B/T$  approximately follow lines of constant bulge luminosity, although, as expected, considerable curvature is observed, considering that the host galaxies of pseudo bulges are generally less massive and less luminous. We find that, along the direction of the Kormendy relation, bulges form a sequence of increasing  $B/T$ , from small  $r_e$  to large  $r_e$ . This again reinforces the point that both classical and pseudo bulges can have small and large  $B/T$ , even if on average classical bulges have larger  $B/T$ .

Pseudo bulges are generally weak, with 78% of them having  $B/T < 0.1$  (Figure 2d). Meanwhile, classical bulges are not always strong; 26% of them have  $B/T < 0.1$ . The distributions of  $B/T$  for classical and pseudo bulges significantly overlap. The mean  $B/T$  of classical bulges is 0.21, not dramatically larger than that of pseudo bulges ( $\langle B/T \rangle = 0.08$ ). Fisher & Drory (2008, hereafter FD08) and Gadotti (2009, hereafter G09) also see such an overlap, but in general their values of  $B/T$ , both of classical and pseudo bulges, are significantly larger than ours (Figure 3). This systematic difference repeatedly shows up when comparing bulge properties derived from two-dimensional (2D) image fitting and one-dimensional (1D) surface brightness profile fitting (see Section 5 of Gao et al. 2019). In Figure 4, we illustrate this effect by comparing our  $B/T$  values with those of FD08 at fixed Hubble type. FD08 find systematically larger  $B/T$  than we do in disks of early to intermediate type, while their values are generally consistent with ours for Hubble types later than Sb. The difference is most dramatic in early-type disks.<sup>2</sup> The trend holds true for both classical and pseudo bulges.

We speculate that the systematic discrepancies between our results and those of FD08 are a direct consequence of the different fitting techniques applied to perform the bulge decomposition and the different input models used. We believe that our 2D fits provide more robust bulge parameters because our multi-component models properly separate the bulge from surrounding and overlapping substructures such as bars and lenses. The 1D approach of FD08 explicitly masks such substructures during the fitting. As shown by Gao & Ho (2017), this introduces large uncertainties in bulge pa-

rameters, especially in early-type disks where such substructures are most prevalent. We find better agreement with G09’s results, presumably because his 2D decomposition technique is similar to ours, as is his criteria for classifying bulges. Nevertheless, the average bulge strength found by Gadotti ( $\langle B/T \rangle = 0.33$  for classical bulges;  $\langle B/T \rangle = 0.15$  for pseudo bulges) is also larger than ours (Figure 3). Although Gadotti’s 2D method is certainly more trustworthy than 1D methods, and it does systematically treat bars, our 2D method (GALFIT; Peng et al. 2002, 2010) can handle a vastly more intricate array of internal substructures (Gao & Ho 2017; Gao et al. 2018, 2019), which ultimately leads to more robust bulge parameters. Kormendy (2016)’s statement that almost all pseudo bulges have  $B/T \lesssim 0.35$  and  $B/T \gtrsim 0.5$  guarantees that the bulge is classical still applies to our measurements, but it is not representative because  $B/T \lesssim 0.2$  already includes most pseudo bulges and few bulges of either type have  $B/T \gtrsim 0.5$ . We echo previous works (e.g., Neumann et al. 2017) that stress that  $B/T$  is not a good parameter to distinguish between classical and pseudo bulges. The two bulge types simply overlap too heavily in  $B/T$ . The implication of such overlap at low  $B/T$  will be discussed in Section 4.3.1.

Although classical bulges are not necessarily prominent, they do mostly have high surface brightnesses (Figure 2e), a direct outcome of their classification based on the Kormendy relation. It is noteworthy that the distribution of  $\langle \mu_e \rangle$  shows the strongest separation between classical and pseudo bulges among all the structural parameters of bulges. A demarcation line at  $\sim 18.5$  mag arcsec<sup>-2</sup> can isolate most of the classical bulges from the pseudo bulges. If any single bulge structural parameter should be used to classify classical and pseudo bulges,  $\langle \mu_e \rangle$  would be the best choice to produce consistent classifications based on the Kormendy relation. Adopting a boundary of  $\langle \mu_e \rangle = 18.5$  mag arcsec<sup>-2</sup> (in the  $R$  band) would correctly classify 87% of the pseudo bulges and 77% of the classical bulges.

S0 galaxies exhibit a wide range of bulge prominence, from traditionally bulge-dominated systems to those with bulges as weak as those in spirals of type Sc and later (Gao et al. 2018). However, in stark contrast to late-type spirals, which host mostly pseudo bulges, the bulges of S0s essentially *all* form a uniform sequence with the ellipticals on the Kormendy relation. In other words, almost all bulges in CGS S0s are classical. Based on this observation, Gao et al. (2018) argue that, unless historically popular processes such as ram-pressure stripping can modify bulge structures substantially, most S0s cannot simply be descendants of faded late-type spirals (later than Sc). The present study further reinforces the

<sup>1</sup> We adopt the implementation of the two-dimensional LOESS method by Cappellari et al. (2013b), who provide the code in <http://purl.org/cappellari/idl>.

<sup>2</sup> The S0/a bin is an exception probably because it contains only two galaxies.

conclusions of Gao et al. (2018). S0 bulges, independent of their  $B/T$ , occupy almost exclusively the upper envelope of the  $\langle\mu_e\rangle - r_e$  plane. The weakest bulges found in S0s ( $B/T \lesssim 0.1$ ) have surface brightnesses at least 2 magnitudes brighter than the majority of the comparably weak bulges in late-type spirals (Figure 2a).

### 3.3. Bimodality or Continuity in Sérsic Indices

Figure 5 shows the distribution of CGS bulges on the Kormendy relation, with symbols color-coded according to their Sérsic indices. We show both the original data (panel a) and the LOESS-smoothed version (panel b) to facilitate visualization of the general trend. Along the direction of the Kormendy relation, bulges in general form a sequence of increasing Sérsic indices, from small to large  $r_e$ . This hints that both classical and pseudo bulge can have small and large Sérsic indices, even if on average classical bulges have larger values. As with G09, we find that a minority of the pseudo bulges have Sérsic indices larger than 2. Meanwhile, a substantial fraction of classical bulges have  $n < 2$  (panel c). Although on average pseudo bulges have smaller Sérsic indices than classical bulges, we do *not* observe the bimodal distribution of Sérsic indices reported in FD08, which was the empirical basis of their Sérsic  $n$ -based classification criterion. FD08 identified pseudo bulges mainly based on their nuclear morphologies (presence of nuclear bars, rings, and spirals). However, the recent analysis of a small sample of double-barred galaxies by de Lorenzo-Cáceres et al. (2019) showed that most of the underlying bulges are classical. Moreover, Tabor et al. (2017) found some pressure-supported bulges in S0s with  $n \approx 1$ . In the same vein, Méndez-Abreu et al. (2018) discuss the lack of clear correspondence between bulge Sérsic index and their kinematics. Costantin et al. (2018) tested various observational diagnostics to separate classical and pseudo bulges and also concluded that Sérsic index is disfavored. Although Sérsic indices do carry physically significant information (e.g., mergers result in higher Sérsic indices: Aguerri et al. 2001; Eliche-Moral et al. 2006; Brooks & Christensen 2016), their large measurement error (Gadotti 2008) and sensitivity to spatial resolution (Balcells et al. 2003) and nuclear fine structures (Gao & Ho 2017) may hamper their application in classifying bulges. Combined with the discrepant classification results mentioned above, we suggest that  $n = 2$  is not an appropriate demarcation line for separating classical and pseudo bulges. As with Neumann et al. (2017), we find that  $n = 1.5$  is a better criterion; based on the statistics of CGS, this revised criterion would correctly classify 65% of the pseudo bulges and 74% of the classical bulges. Note that even with this modified threshold

Sérsic  $n$  is still a less effective classifier of bulge type than  $\langle\mu_e\rangle$  (Section 3.2).

We also compare the distribution of bulge Sérsic  $n$  from CGS with those from FD08 and G09 (Figure 6). It is evident that both our measurements and those of G09 show significant overlap in  $n$  for classical and pseudo bulges, while in FD08 the two bulge types are well separated at  $n \approx 2$ . In contrast to the comparison of  $B/T$  at fixed Hubble type (Figure 4), Figure 7 shows that FD08’s measurements show no noticeable systematic difference in bulge Sérsic  $n$  at fixed Hubble type for all bulges. This is also true for pseudo bulges. However, our values of  $n$  are systematically larger than those in FD08 for classical bulges in galaxies of all Hubble types.

### 3.4. Classical and Pseudo Bulges Share Similar Relative Bulge Size

Our decomposition demonstrates that classical and pseudo bulges have similar relative bulge size ( $2r_e/D_{25}$ ), contrary to the results of FD08, who found that classical bulges have significantly larger relative sizes than pseudo bulges (Figure 8). We use  $D_{25}$  from Ho et al. (2011) for CGS galaxies and retrieve  $D_{25}$  of the sample in FD08 from HyperLeda<sup>3</sup> (Paturel et al. 2003). To investigate the origin of the discrepant results, we plot  $2r_e/D_{25}$  as a function of Hubble type and  $B/T$  in Figure 9. We find that at fixed Hubble type or  $B/T$ , bulges in CGS and FD08 have similar mean relative bulge size, which increases as  $B/T$  increases; except for early-type disks (S0 and Sa), FD08’s measurements are systematically larger than ours. It is also noteworthy that in the case of CGS, at a fixed  $B/T$ , pseudo bulges are more diffuse (larger  $2r_e/D_{25}$ ) than classical bulges. It is evident in Figure 3 that the separation of  $B/T$  of classical and pseudo bulges in CGS is much less significant than in FD08. Therefore, we speculate that the discrepant bulge relative size distributions of classical and pseudo bulges between CGS and FD08 is mainly due to the discrepant  $B/T$  measurements for the two populations of bulges.

### 3.5. Bulge Dichotomy in Their Intrinsic Shapes

Intrinsic shapes of bulges have been extensively investigated by Méndez-Abreu et al. (2008, 2010), Costantin et al. (2017, 2018), and de Lorenzo-Cáceres et al. (2019). Without constraints from stellar kinematics, however, it is extremely difficult to measure the intrinsic shapes of individual bulges. Instead of looking into the intrinsic shapes, we turn to examining the statistics of their intrinsic flattenings. Figure 10 presents the apparent el-

<sup>3</sup> <http://leda.univ-lyon1.fr/>

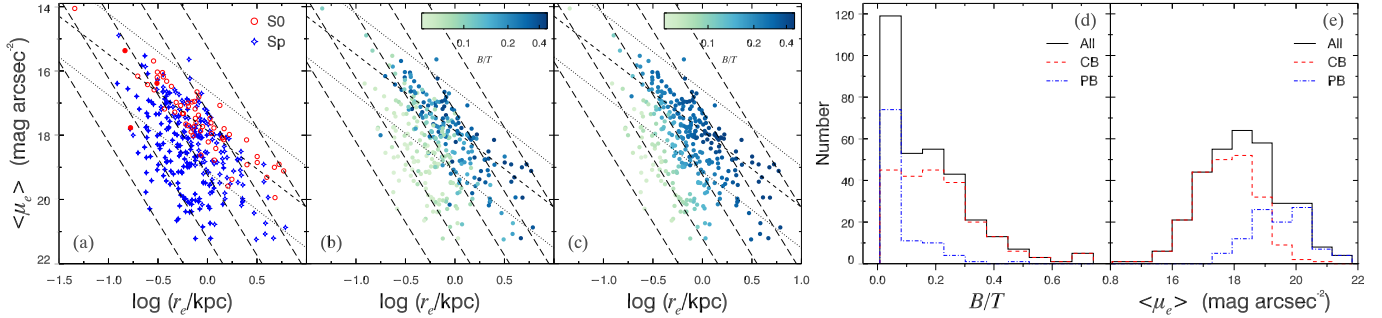


**Figure 2.** Bulges in the Kormendy relation: (a) distinguished by Hubble types, (b) color-coded according to their  $B/T$ , and (c) LOESS-smoothed version of panel (b). The filled symbols in panel (a) represent weak bulges ( $B/T < 0.1$ ) in S0s (red) and spirals (blue). The best-fit relation and its  $3\sigma$  boundary of the ellipticals are indicated by the short-dashed lines and dotted lines, respectively. The long-dashed lines approximately represent trajectories of constant bulge luminosities (ignoring cosmological effects). Panel (d) displays the distribution of  $B/T$  for the classical (red) and pseudo (blue) bulges; the overlap is significant. The two bulge types are better distinguished in surface brightness (e).

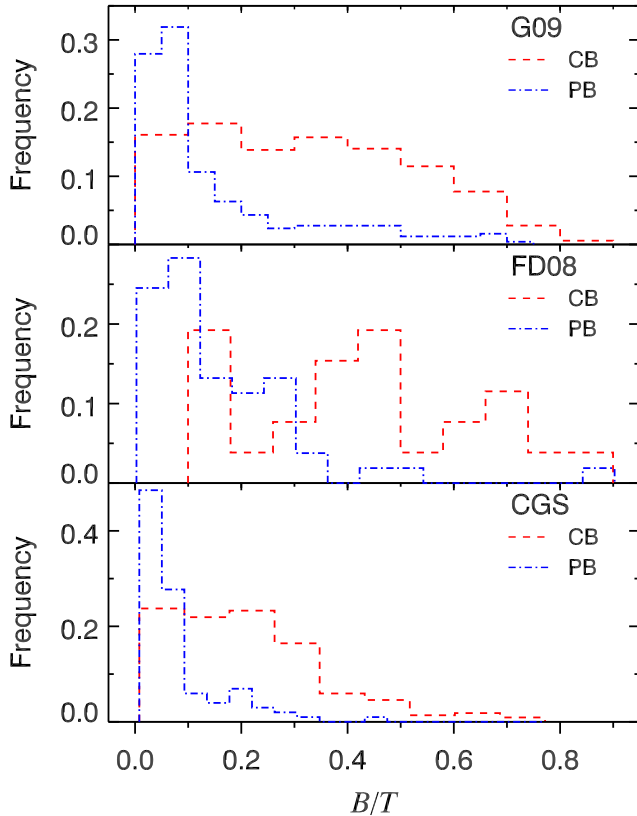


**Figure 3.** Distributions of  $B/T$  for classical (red) and pseudo (blue) bulges in (top) G09, (middle) FD08, and (bottom) CGS.

lpticity ( $\epsilon$ ) distributions of classical and pseudo bulges. Classical bulges are on average apparently rounder than pseudo bulges. The two distributions are statistically different. A Kolmogorov-Smirnov test rejects the null hypothesis that the two samples are drawn from the same population at a probability of  $P_{\text{null}} \approx 10^{-4}$ . The distribution of the apparent ellipticities of classi-

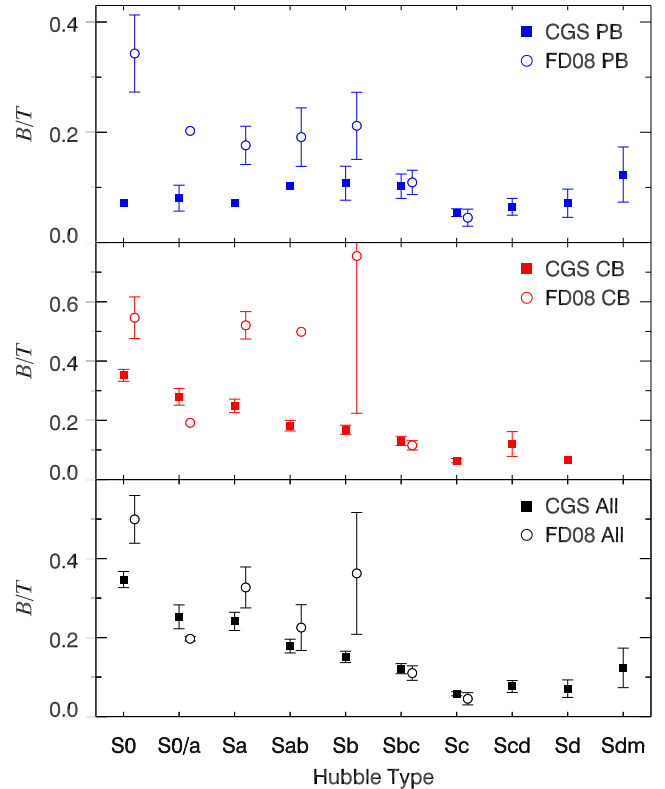


**Figure 4.** Distributions of  $B/T$  as a function of Hubble type in this study (CGS) with those from FD08 for (top) pseudo bulges, (middle) classical bulges, and (bottom) both bulge types combined. Symbols and error bars represent mean and error of the mean in each bin. Symbols are horizontally offset for clarity.

cal bulges is skewed markedly toward small ellipticities, while pseudo bulges have a broader distribution, reminiscent of the difference between apparent ellipticities of disks and spheroids (Sandage et al. 1970). Overlaying the apparent ellipticity distributions of CGS ellipticals

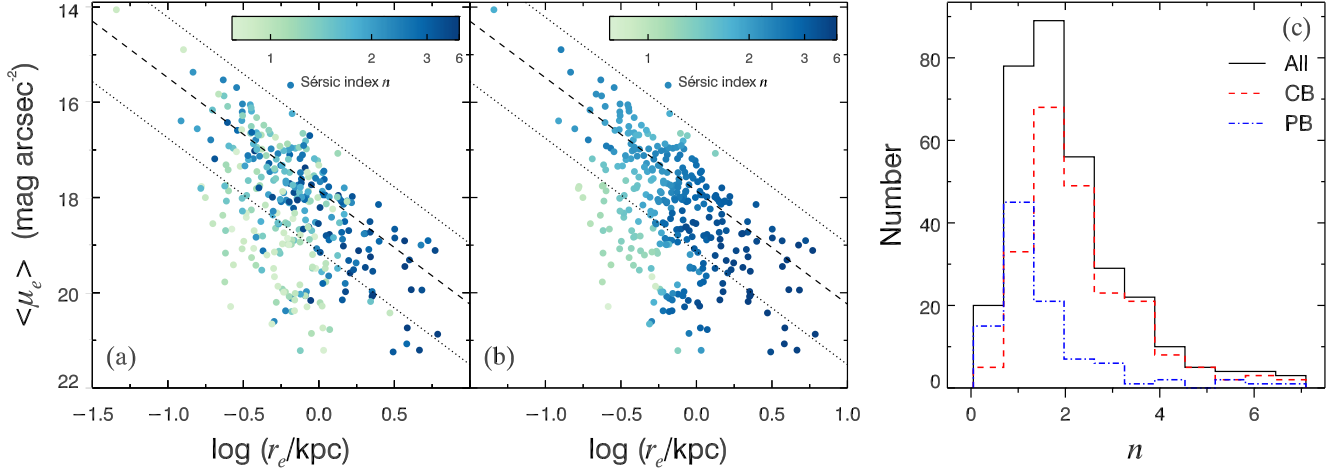


**Figure 5.** (a) Bulges in the Kormendy relation color-coded according to their Sérsic indices. Panel (b) is the same as panel (a), but the data have been LOESS-smoothed. The best-fit relation and its  $3\sigma$  boundary of the ellipticals are indicated by short-dashed lines and dotted lines, respectively. Panel (c) shows the distribution of Sérsic indices for the classical (red) and pseudo (blue) bulges. The overlap is significant, and the bimodality presented in FD08 is not observed here.

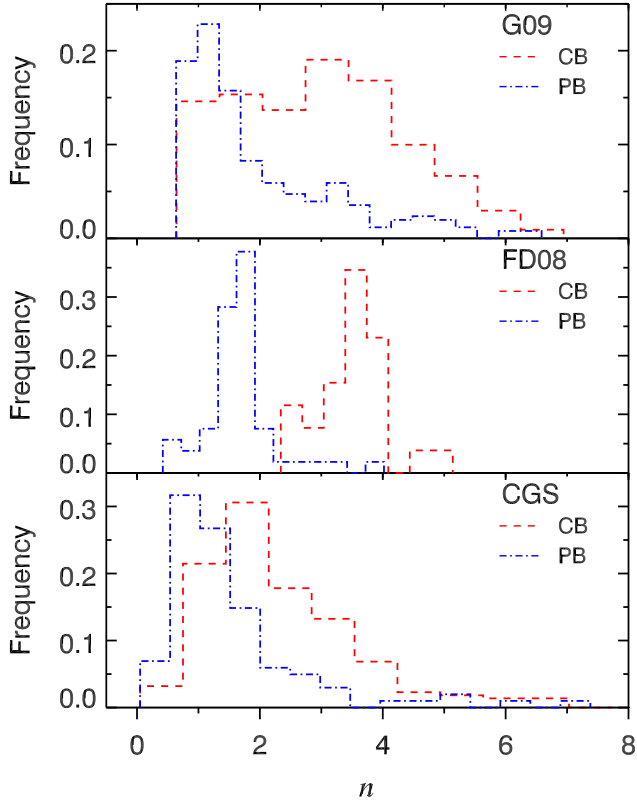


**Figure 6.** Distributions of Sérsic  $n$  for classical (red) and pseudo (blue) bulges in (top) G09, (middle) FD08, and (bottom) CGS.

and disk galaxies from Ho et al. (2011) reveals that classical bulges have similar apparent ellipticities with ellipticals while the apparent ellipticities of pseudo bulges closely resemble those of disk galaxies. This is formally confirmed from Kolmogorov-Smirnov tests of the four

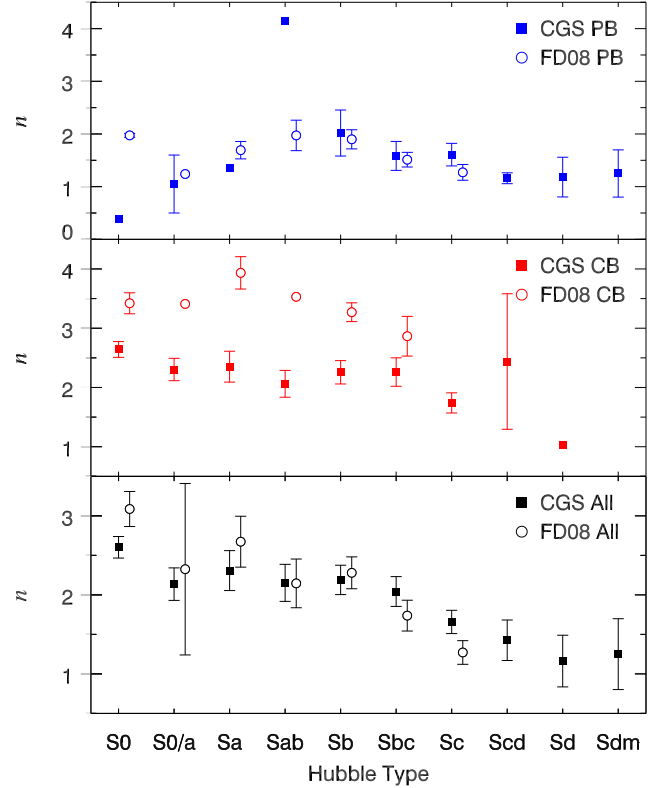


**Figure 7.** Distributions of bulge Sérsic  $n$  as a function of Hubble type in this study (CGS) with those from FD08 for (top) pseudo bulges, (middle) classical bulges, and (bottom) both bulge types combined. Symbols and error bars represent the mean and error of the mean in each bin. Symbols are horizontally offset for clarity.

populations:  $P_{\text{null}} = 0.51$  for classical bulges vs. ellipticals;  $P_{\text{null}} = 0.27$  for pseudo bulges vs. disk galaxies. Classical bulges are intrinsically as round as ellipticals,



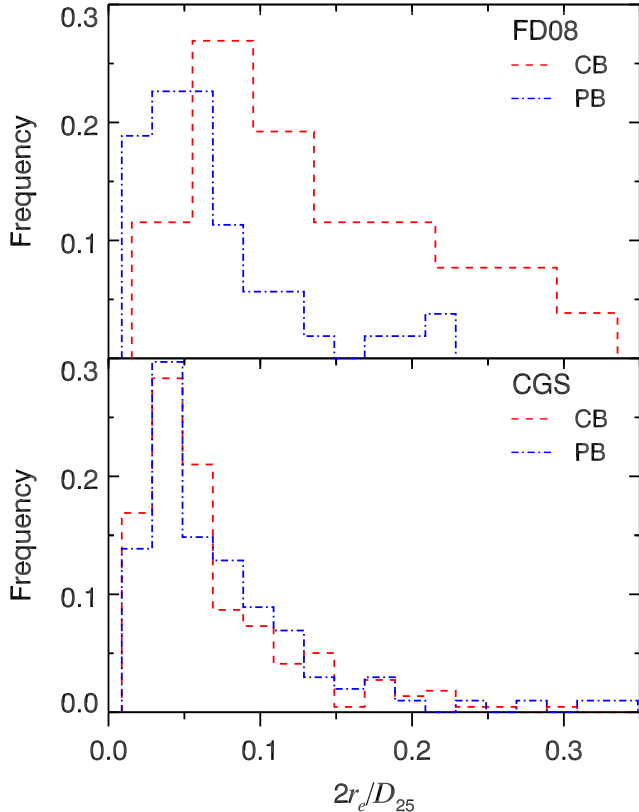


**Figure 8.** Distributions of relative size of classical (red) and pseudo (blue) bulges in (top) **FD08** and (bottom) **CGS**. The bulge effective radius  $r_e$  is normalized to the  $D_{25}$  isophotal diameter of the galaxy.

and pseudo bulges are intrinsically as flattened as disks. This is consistent with the picture that classical bulges were formed in a manner similar to that of ellipticals, while pseudo bulges originate from the gradual accumulation of disk material, having preserved enough memory of their disky origin to be recognized. However, as the apparent ellipticities of the two populations overlap with each other due to projection effects, we do not suggest using ellipticity as a criterion to separate classical and pseudo bulges.

### 3.6. Dichotomies in Classical and Pseudo Bulge Hosts

Section 3.5 shows that pseudo bulges are basically miniature disks. As disks are vulnerable to violent processes such as mergers, pseudo bulges are most likely to be found in late-type spirals, whose evolutionary history has been driven more by secular evolution than major mergers. Figure 11 examines the dependence of pseudo bulge incidence on Hubble type, stellar mass  $M_*$ , and  $B-V$  color. As expected, pseudo bulges are more frequent in galaxies with later Hubble types, lower stellar masses, and bluer optical colors. We also contrast the

pseudo bulge incidence in barred and unbarred galaxies, but find no systematic differences between the two subsamples. This is counterintuitive, because bars are often thought to be the main driver of secular evolution. We will elaborate on this point in the next section.

In broad agreement with the literature, we also find that pseudo bulges prefer to reside in late-type spirals. Spirals with Hubble types later than Sbc are indeed the most active manufacturing sites of pseudo bulges. At least  $\sim 60\%$  of them host pseudo bulges. However, our pseudo bulge incidence in most Hubble types is significantly smaller than previously found. [Kormendy & Kennicutt \(2004\)](#) summarized the statistics of pseudo bulges as a function of Hubble type from the literature. Based on morphologies and Sérsic indices of 75 galaxies with *Hubble Space Telescope (HST)* images analyzed by [Carollo et al. \(1997\)](#), they found that 69%, 50%, 22%, 11%, and 0% of S0–Sa, Sab, Sb, Sbc, and Sc and later type galaxies host classical bulges, respectively. The general trend of increasing incidence of pseudo bulges toward late Hubble types is consistent with our measurements. However, their pseudo bulge fraction is higher than ours (Table 1). The same holds true for the work of [Kormendy & Kennicutt \(2004\)](#), who, re-analyzing the sample of [Carollo et al. \(2002\)](#) based on *HST V*-band and *H*-band images, concluded that 50%, 40%, 56%, 94%, and 100% of S0+Sa, Sab, Sb, Sbc, and Sc–Sm galaxies host exponential bulges. Exponential bulges are considered a close proxy for pseudo bulges. Taken at face value, their pseudo bulge fraction is again systematically higher than ours. We do not know the exact reason of the quantitative discrepancy, as differences in bulge-to-disk decomposition techniques, wavelength effects, spatial resolution of the data, sample size (CGS is significantly larger than the above-cited samples), and, more directly, the classification criteria affect the outcome.

### 3.7. Pseudo Bulges and Their Relation to Bars

In Section 3.6 we already noted that barred galaxies do not host more pseudo bulges than unbarred galaxies at fixed Hubble type, stellar mass, or optical color. This is unexpected, if bars drive secular evolution, as is often surmised (e.g., [Kormendy & Kennicutt 2004](#); [Wang et al. 2012](#); [Lin et al. 2017](#); [Chown et al. 2019](#)). Figure 12 investigates this issue in the context of the Kormendy relation. Again, we find no indication that the presence of a bar has any effect on skewing objects below the Kormendy relation of the ellipticals (i.e., toward the locus of pseudo bulges). This seems to be in conflict with the notion that bars help drive gas inflow and to build pseudo bulges. However, one should bear in mind that bars can also contribute to bulge growth

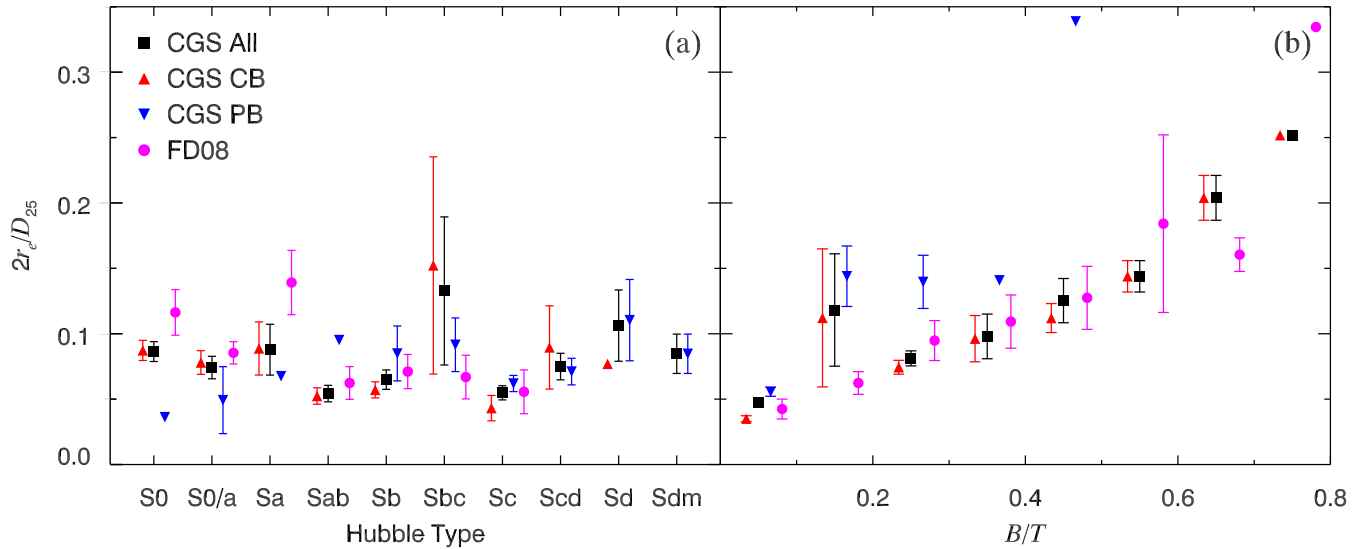


**Figure 9.** Relative size of the bulge as a function of (a) Hubble type and (b)  $B/T$  for all CGS bulges (black), CGS classical bulges (red), CGS pseudo bulges (blue), and bulges in FD08 (magenta). The bulge effective radius  $r_e$  is normalized to the  $D_{25}$  isophotal diameter of the galaxy. Symbols and error bars represent mean and error of the mean in each bin, respectively. Symbols are horizontally offset for clarity.

**Table 1.** Percentage of Pseudo Bulge Hosts in Bins of Hubble Type and Stellar Mass

| Hubble Type        | S0          | S0/a        | Sa          | Sab       | Sb         | Sbc        | Sc          | Scd         | Sd          | Sdm         |
|--------------------|-------------|-------------|-------------|-----------|------------|------------|-------------|-------------|-------------|-------------|
| All                | $2 \pm 2$   | $13 \pm 9$  | $4 \pm 4$   | $4 \pm 4$ | $28 \pm 6$ | $32 \pm 6$ | $62 \pm 7$  | $79 \pm 8$  | $88 \pm 12$ | $100 \pm 0$ |
| Barred             | $0 \pm 0$   | $9 \pm 9$   | $10 \pm 10$ | $7 \pm 6$ | $15 \pm 7$ | $33 \pm 9$ | $55 \pm 11$ | $82 \pm 12$ | $100 \pm 0$ | $100 \pm 0$ |
| Unbarred           | $3 \pm 3$   | $25 \pm 22$ | $0 \pm 0$   | $0 \pm 0$ | $40 \pm 9$ | $31 \pm 9$ | $67 \pm 8$  | $77 \pm 12$ | $67 \pm 27$ | $100 \pm 0$ |
| $\log M_*/M_\odot$ | 8.5–9.5     |             | 9.5–10.0    |           | 10.0–10.5  |            | 10.5–11.0   |             | 11.0–12.0   |             |
| All                | $100 \pm 0$ |             | $72 \pm 7$  |           | $47 \pm 5$ |            | $10 \pm 3$  |             | $0 \pm 0$   |             |
| Barred             | $100 \pm 0$ |             | $67 \pm 12$ |           | $41 \pm 8$ |            | $9 \pm 4$   |             | $0 \pm 0$   |             |
| Unbarred           | $100 \pm 0$ |             | $75 \pm 9$  |           | $54 \pm 7$ |            | $13 \pm 4$  |             | $0 \pm 0$   |             |

through dissipationless processes, most notably via the buckling instability. The difference in formation physics between bar buckling instability and bar-driven gas inflow motivated Athanassoula (2005) to advocate that boxy/peanut bulges should be regarded as a separate class from other pseudo bulges. The bulge-like structure produced by bar buckling instability is not necessarily weak (small  $B/T$ ) or disky (small  $n$ ). This is illustrated in Figure 12, where the bulges of buckled barred galaxies occupy the locus of classical bulges with large  $n$  ( $\gtrsim 2$ ) and  $B/T$  ( $\gtrsim 0.2$ ). The classifications of the buckled bars come from Li et al. (2017), who visually identified boxy/peanut bulges and barlenses, both of which are regarded as the same phenomena viewed from different inclination angles, based on variations of isophotal shapes in the bar region. We conclude that the Kor-

mendy relation mostly only selects pseudo bulges that are formed from dissipative secular processes. We do not know whether this is because of the inherent limitations of the Kormendy relation—given its substantial intrinsic scatter—or because bulges with buckled bar features are not genuine pseudo bulges. We observed a similar phenomenon before (Gao et al. 2018). The bulges of some S0 galaxies bear the appearance of pseudo bulges but are not recognized as such on the Kormendy relation. Disky features do not reliably signify the overall photometric structure or the star formation activities of the bulge. Given that buckled bars occur most frequently in early-type disks, where mergers were once operative, they may not dominate the overall bulge structure.

Bars play a critical role in facilitating gas inflow, the raw material for star formation in galaxy centers and

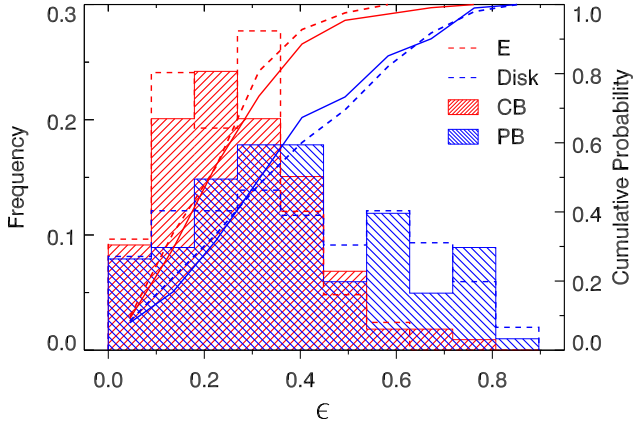


**Figure 10.** Distributions of apparent ellipticities of classical (red) and pseudo (blue) bulges, CGS ellipticals (red dashed), and CGS disks galaxies (blue dashed). The cumulative probability of each subgroup is overlaid with the same line style.

hence for pseudo bulge growth. It is instructive to control for the amount of available gas and then compare pseudo bulge properties of barred and unbarred galaxies. While we expect the pseudo bulge fraction to increase toward more gas-rich galaxies, a natural consequence of the increase of specific gas content toward galaxies with higher specific star formation rate and later Hubble type (Roberts & Haynes 1994, and references therein), more available gas does not seem to be related to increased pseudo bulge fraction for barred galaxies (Figure 13). At fixed gas fraction, the pseudo bulge fraction of barred galaxies is not significantly different than that of unbarred galaxies. If there is any systematic trend at all, it goes in the opposite direction. Bulge prominence ( $B/T$ ) and normalized bulge size ( $2r_e/D_{25}$ ) of pseudo bulges do not show any systematic trends with gas content, while Sérsic  $n$  seems to increase toward gas-poor galaxies, but the results are inconclusive because of the small number statistics in the three most gas-poor bins. Again, at fixed gas fraction, the presence of a bar has no relation to  $B/T$ , Sérsic  $n$ , or  $2r_e/D_{25}$ . Due to the small number statistics, we cannot afford to further control for galaxy stellar mass, but comparison of the stellar mass distribution of barred and unbarred galaxies rules out stellar mass as an important factor. If barred galaxies were to host more and stronger pseudo bulges, then, to account for the similar pseudo bulge properties of barred and unbarred galaxies we would expect the stellar masses of barred galaxies to deviate systematically from those of unbarred galaxies. Comparison of the stellar masses of barred and unbarred galaxies at fixed gas fraction does not reveal any systematic differences.

To summarize: pseudo bulges identified by the Kormendy relation rarely include bulges with boxy/peanut features (or barlenses when viewed face-on). Therefore, the pseudo bulges identified in this paper largely refer to those formed out of material accumulated from central gas inflows, not from the bar buckling instability. We find no evidence that at a fixed gas fraction bars help the formation or growth of pseudo bulges. Implications of these results will be addressed in Section 4.3.2.

## 4. DISCUSSION

### 4.1. Bulge Definition: Comparison with Previous Studies

Measurements of bulge parameter depend on which part of the galaxy is regarded as the bulge. As illustrated in Gao & Ho (2017) and Gao et al. (2018, 2019), we consistently adopt the convention that bulges refer to extra light above the inner extrapolation of disks/bars, after excluding any possible nuclei. Note that disks here do not necessarily refer to a single exponential component but instead to the analytic function or combination of functions that best describes the disk surface brightness. Therefore, the bulge component includes the contribution from nuclear bars/rings and boxy/peanut bulges (thickened part of bar), if present. We do not model these substructures as individual, separate components in addition to the bulge, although some are actually part of the bar (e.g., boxy/peanut bulges). If we model all distinct disky features in the bulge region as individual components, we risk isolating every pseudo component from the rest of the photometric bulge. This betrays our goal to characterize bulge dichotomies in the local Universe. We acknowledge that other studies with different scientific goals may adopt different bulge definitions from ours, and therefore their bulge parameters may not be comparable to ours. For example, Läsker et al. (2016) isolated everything else to extract the pure classical bulges to study black hole–bulge relations. The study of de Lorenzo-Cáceres et al. (2019) modeled nuclear bars separately because the latter were the objects of interest. In the same vein, we adopt the definition that best suits our specific goal, which is to characterize the structural properties of the overall photometric bulge, no matter how many subcomponents it might have. Our definition is similar to that of G09, only that our disk models are more detailed than his, causing the bulge parameters to be different (Figure 3).

FD08 employed a different method than we to measure bulge parameters. Due to the limitations of their 1D technique, non-axisymmetric components (e.g., bars and lenses) cannot be modeled simultaneously with the bulge and disk, and FD08 excluded them from the fit.

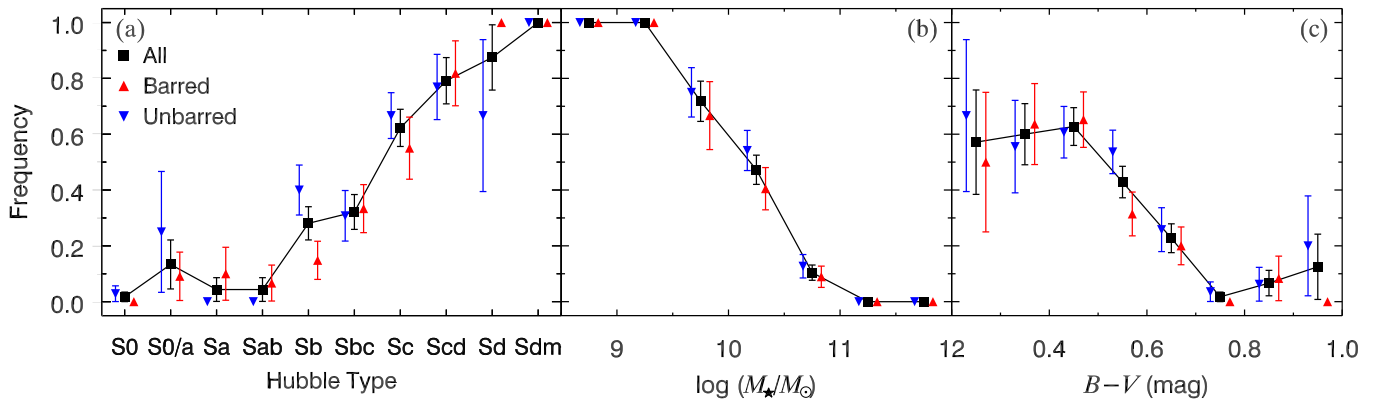


**Figure 11.** Frequency of pseudo bulges as a function of the (a) Hubble type, (b) stellar mass, and (c) optical color of the host galaxy. Black symbols with connected lines represent all galaxies, and red and blue symbols are barred and unbarred galaxies, respectively. Error bars are calculated assuming a binomial distribution. Symbols are horizontally offset for clarity.

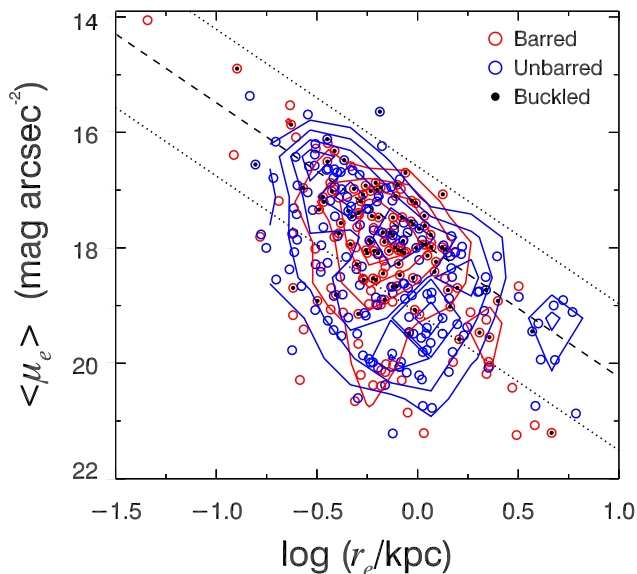


**Figure 12.** Bulges on the Kormendy relation for barred (red) and unbarred (blue) galaxies. The buckled bars recognized by Li et al. (2017) are marked by solid black dots; due to different strategy of identifying barred galaxies, some of the buckled bars are designated unbarred according to the classification of this paper. The best-fit relation and its  $3\sigma$  boundary of the ellipticals are indicated by short-dashed lines and dotted lines, respectively. The barred and unbarred galaxies do not show any preference to host classical/pseudo bulges. Most of the boxy/peanut bulges follow the Kormendy relation of the ellipticals.

Their bulge definition also differs subtly from ours, as they masked nuclear rings/bars from their fits. This might affect bulge structural parameters but should not alter  $B/T$  much (Gao & Ho 2017; de Lorenzo-Cáceres et al. 2019). To better understand the underlying reasons for the discrepancy between our results and those of FD08, we closely examined the 14 galaxies in common between the two samples. Fortunately, none of the

galaxies contains complications from nuclear disk features, affording a relatively straightforward comparison between FD08’s technique and ours.

Figure 14 illustrates the bulge-dominated region for the overlapping objects. Because FD08 did not provide the position angles of their bulges, we assume that their values are the same as ours. We find that except for NGC 1022 and NGC 3521 where FD08’s bulges are treated as nuclei in our fits, both studies ascribe the same physical entity to the bulge. The discrepancies in the resulting bulge parameters mostly reflect differences in data quality, in the techniques applied, and in details of the model construction. Our 2D approach generally allows for more direct and robust model construction to account for the multicomponent nature of nearby disk galaxies.

Figure 15 compares the bulge parameters from this study with those from FD08 for the comparison sample. Taking into consideration the large uncertainties of the parameters in FD08, their measurements, apart from a few outliers, are broadly consistent with ours, and there are no significant systematic trends. Unfortunately, the small size of the comparison sample precludes us from drawing any firm conclusions as to the origin of the systematic discrepancies in  $B/T$  and relative bulge size of early-type disks. Among the 14 galaxies in common, there are only two Sa galaxies, one Sa/0 galaxy, and no S0s, where the differences in  $B/T$  and relative bulge size are most significant. As mentioned above, various reasons could be responsible for the differences. Our smaller  $B/T$  in early-type disks, where classical bulges are most abundant, in conjunction with our classification criterion that includes less prominent classical bulges (small  $n$ ), results in a less clear separation between classical and pseudo bulges in the  $B/T$  distribution, when compared with FD08 (Figure 3). This leads to both bulge types having similar relative sizes

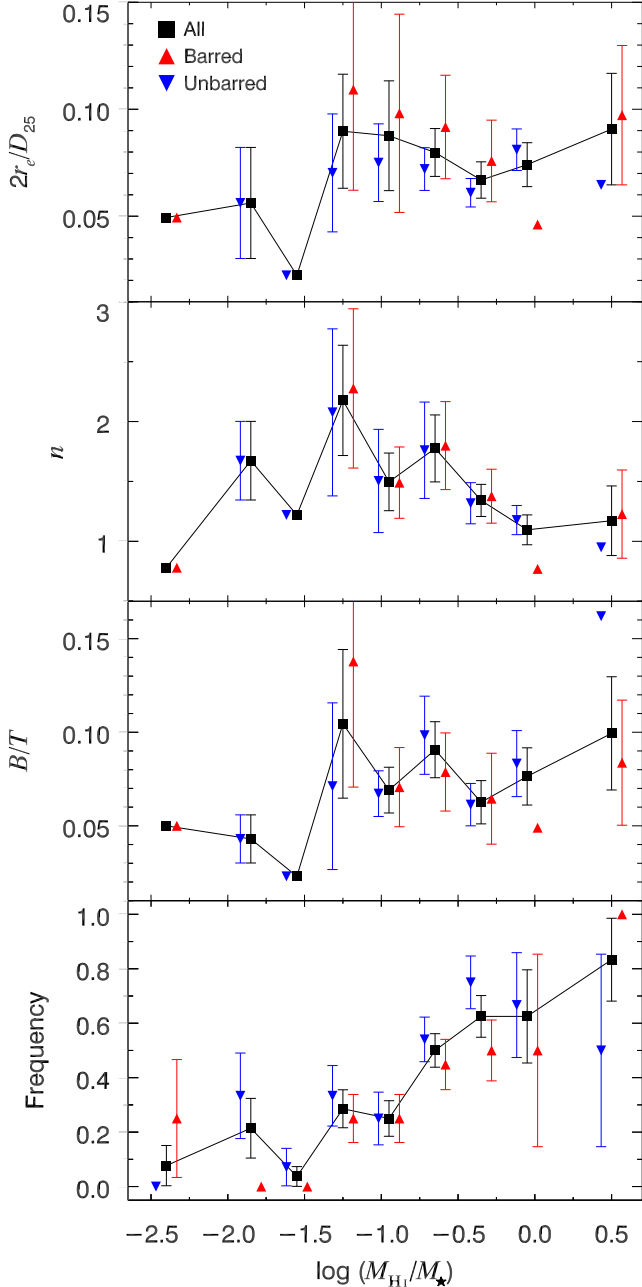


**Figure 13.** Correlation of pseudo bulge properties with the gas fraction of their hosts. From top to bottom, the panels show normalized pseudo bulge sizes, Sérsic indices, bulge-to-total ratios, and detection frequency as a function of H I gas fraction, for all galaxies (black), barred galaxies (red), and unbarred galaxies (blue). There are no systematic differences between barred and unbarred galaxies. Errors of pseudo bulge frequency are calculated assuming a binomial distribution. Symbols and error bars in the other panels represent mean and error of the mean in each gas fraction bin, respectively. Symbols are horizontally offset for clarity.

(Figure 8), as argued in Section 3.4. We did not find substantial systematic differences in bulge Sérsic  $n$ , neither for the full sample at fixed Hubble type (Figure 7) nor for the subset of galaxies in common between CGS and FD08 (Figure 15b). Therefore, the significantly different distributions of  $n$  (Figure 6) are probably due to the different classification criteria used by us and FD08.

We also note that the consistency of the classifications is poor. Only four of the 14 bulges have consistent classifications. If we adopted  $n = 2$  to separate classical and pseudo bulges in CGS, our classifications would agree much better with those of FD08 (10/14). This suggests that adopting different classification criteria is the major source of the inconsistency. In contrast to our study that relies on scaling relations, FD08 used nuclear morphologies to distinguish bulge types. While such an approach is physically meaningful and has the merit of being immune from potential bias in bulge structural parameters, it is not quantitative, relying on subjective, visual morphological classification. Moreover, it may not work well in composite bulges whose disk features are not fundamental to the overall bulge nature (e.g., Erwin et al. 2015; Gao et al. 2018).

On the other hand, Kormendy (2013, 2016) and Fisher & Drory (2016) warned against using the Kormendy relation to identify pseudo bulges, because high-density pseudo bulges would risk being misclassified. Given that scaling relations are demonstrated useful in distinguishing objects of different nature, an immediate question is why pseudo bulges should follow the scaling relation of ellipticals. A plausible explanation is that these are composite bulges, which contain contributions from secular evolution and therefore can be recognized using Sérsic index or nuclear morphology. Unfortunately, this issue cannot be resolved in the context of a binary classification scheme, namely classifying bulges as either classical or pseudo bulges. In such an exercise, without independent measurements of the relative importance of violent to secular processes in bulge growth, it is difficult to tell which criterion is superior. However, it is possible to assess the robustness of such classifications. For example, as mentioned in Section 1, Neumann et al. (2017) have done so by comparing various bulge type indicators and found that using the Kormendy relation alone can recover classifications based on multiple criteria to a high success rate. Without access to other measurements that are useful to classify bulge types (e.g., stellar kinematics and stellar populations), we are unable to follow such a strategy. But we add to their advocacy by showing that pseudo bulges selected by the Kormendy relation exhibit properties that consistently

imply a disk origin and that Sérsic index is not an appropriate indicator of bulge types.

Using the classifications from [FD08](#) for the comparison sample, we find that 30% of the pseudo bulges have  $n > 2$  in CGS, and 25% of the classical bulges have  $n < 2$  in CGS; in [FD08](#), all the pseudo bulges have  $n < 2$ , and all the classical bulges have  $n > 2$ . This suggests that differences in Sérsic  $n$  measurements tend to weaken the separation of  $n$  of classical and pseudo bulges in CGS. The next section will demonstrate that the weakening of the bimodality is not due to the relative large number of classical bulges in the CGS sample.

To summarize: the small number of overlapping galaxies precludes us from investigating the cause of the discrepancies between our study and that of [FD08](#). We speculate that differences in data quality, fitting techniques, model construction, and classification criteria all play a role.

#### 4.2. Conflicts with Previous Results

Some of our population statistics differ from those of previous studies (Sections 3.2, 3.3, 3.4, and 3.6). First, the basis of the widely adopted criterion for bulge classification—the bimodal distribution of Sérsic indices—cannot be reproduced in our measurements. Does the discrepancy stem merely from the different methods used to classify bulge type? After all, [FD08](#) identified pseudo bulges based on their nuclear morphologies in *HST* images, while we define pseudo bulges as low-surface brightness outliers in the Kormendy relation.

We do not think that this can be the whole story. If we suppose that classical and pseudo bulges have distinct distributions in Sérsic index and can be well separated at  $n \approx 2$ , we would have 125 classical bulges and 195 pseudo bulges in CGS, similar to but slightly different from the relative numbers in [FD08](#) (26 vs. 53). On the contrary, the [G09](#) sample is dominated by  $n \geq 2$  bulges (421 vs. 267). The different relative number of classical to pseudo bulges could erase the bimodality in the global distribution of bulge Sérsic index. We explore the effects of varying the relative fraction of classical to pseudo bulges on the global distribution of bulge Sérsic index in the [FD08](#) sample, by matching the statistics of CGS and [G09](#). Following the style presented in Figure 9 of [FD08](#), we plot the distribution of  $\log n$  in Figure 16. Although we observe a gentle dip at  $\log n \approx 0.3$  for CGS (unfilled black histogram), it is still not comparable with the significant deficit of bulges in the [FD08](#) sample at  $\log n \approx 0.4$  (filled black histogram), after matching the relative number of classical to pseudo bulges. The same holds for the comparison of the [G09](#) sample (unfilled red

histogram) with the [FD08](#) sample (filled red histogram). There is always a strong dip at  $\log n \approx 0.4$  for the [FD08](#) sample, no matter whether it is dominated by classical or pseudo bulges. In concert with the comparisons for the objects in common (Figure 15) and at fixed Hubble type (Figure 7), we suspect that the small sample size and selection effects of the [FD08](#) sample may be responsible for their deficit of bulges with  $n \approx 2 - 3$ .

Instead, among all the bulge structural parameters considered in CGS, the clearest separation between classical and pseudo bulges is seen in  $\langle \mu_e \rangle$ . This, of course, is a natural outcome of using the Kormendy relation to classify bulges. A clean separation in  $\langle \mu_e \rangle$  is ensured because pseudo bulges happen to have a similar range of  $r_e$  as classical bulges. Thus,  $\langle \mu_e \rangle$  is an effective single criterion for classifying bulge types consistent with classifications based on the Kormendy relation.

Second, we reiterate that 1D fitting systematically overestimates bulge luminosities (see also Section 5 of [Gao et al. 2019](#)). Early 1D studies often adopted a [de Vaucouleurs \(1948\)](#) law ( $n = 4$ ) for the bulge component, which was later shown to overestimate the bulge contribution (e.g., [Kent 1985](#); [Kodaira et al. 1986](#); [Simien & de Vaucouleurs 1986](#)). [FD08](#) presented significantly improved 1D fitting results by adopting better model assumptions and carefully masking morphological features that deviate from their simplified model. Still, comparison of our results with those from [FD08](#) shows that this effect, most severe in early-type disk galaxies, together with the different classification criteria applied, leads to significant differences between their  $B/T$  distributions and ours, both for classical and pseudo bulges. The same holds for bulge sizes. Whereas we find that classical and pseudo bulges have similar relative sizes, [FD08](#) concluded that the former have larger relative sizes than the latter (Section 3.4). 1D fitting comes with several ambiguities and inherent weaknesses that cannot be overcome (see Section 1 of [Gao & Ho 2017](#) for an overview). The most serious limitation of the 1D technique is that it does not utilize the full 2D spatial information in the image and therefore does not account for the full range of complexity intrinsic to most galaxy disks. Sub-structures such as bars and lenses cannot be adequately modeled in 1D fitting and therefore cannot be isolated properly from the bulge, often causing the bulge to be overestimated (e.g., [Kent 1985](#); [Kodaira et al. 1986](#); [Simien & de Vaucouleurs 1986](#)). Although [FD08](#) strived to mask these features in their fits, [Gao & Ho \(2017\)](#) showed that such a compromised strategy amplifies uncertainties in the resulting bulge parameters due to further loss of information. Our results agree better with those of [G09](#), whose methodology, like ours, can

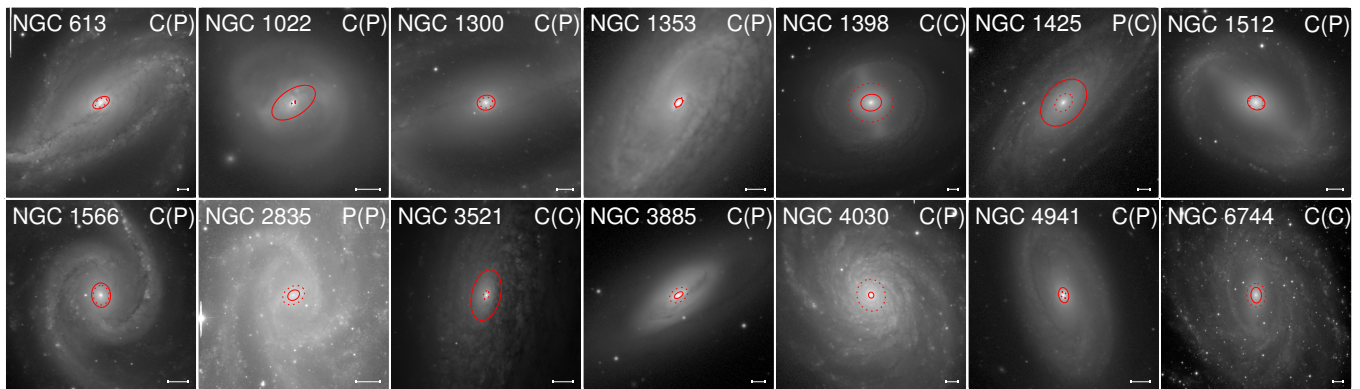


**Figure 14.** *R*-band images of 14 CGS galaxies in common with the FD08 sample. The bulge region is overlaid with a red ellipse (solid = CGS; dashed = FD08), whose semi-major axis represents the bulge effective radius, with axis ratio and orientation following the best-fit model. Bulge types are indicated in the upper-right corner of each image (C = classical; P = pseudo); the classification from FD08 is given in parentheses. The scale bar on the lower-right corner represents 1 kpc.

account for bars. Indeed, we employ the latest version of GALFIT to treat a variety of other sub-structures as well (Gao & Ho 2017). Therefore, we conclude that our measurements, based on better technique and more realistic models, are more accurate than published 1D fitting results, and the differences mostly reflect improvement of measurements.

Finally, we derive a lower pseudo bulge fraction in early-type disks than in studies that use nuclear morphologies and/or Sérsic indices to classify bulges (Figure 11; Section 3.6). This mismatch is probably largely related to differences in classification criteria. We have already noted inconsistencies between classifications based on nuclear morphologies with those based on the Kormendy relation (Figure 3 of Gao et al. 2018). S0 bulges bearing disk features such as nuclear bars and rings cannot be distinguished from classical bulges in terms of their location on the Kormendy relation. We attributed this apparent inconsistency to the fact that the bulges bearing disk features in early-type disks are most likely composite bulges, the bulk of whose mass was assembled early and fast, and secular processes subsequently superposed disk features on top of a pre-existing classical bulge. The disk features also help to lower the Sérsic index of the bulge (see the case of NGC 1326 in Section 4.7 of Gao & Ho 2017). In our estimation, bulge classifications based on the Kormendy relation are more secured than those that rely on nuclear morphology, which neither comprehensively nor reliably signifies the overall photometric structure and formation history of the bulge (see also Fisher et al. 2009).

### 4.3. Implications for Bulge Formation and Evolution

#### 4.3.1. Violent vs. Secular Processes

We summarize the key results from this study that are useful to diagnose the nature of bulges:

- Most pseudo bulges have  $B/T \lesssim 0.1$  and low surface brightness ( $\langle \mu_{e,R} \rangle \gtrsim 18.5 \text{ mag arcsec}^{-2}$ ), while classical bulges have a broad distribution of  $B/T$  and exhibit higher surface brightness ( $\langle \mu_{e,R} \rangle < 18.5 \text{ mag arcsec}^{-2}$ ).
- Pseudo bulges have low Sérsic indices ( $n \lesssim 2$ ), while classical bulges have a broad distribution of  $n$ .
- Classical bulges have an ellipticity distribution consistent with that of elliptical galaxies, while pseudo bulges have a broad distribution of ellipticity reminiscent of disks.
- Pseudo bulges preferentially reside in late-type spirals that are less massive and more gas-rich.

The above-listed properties consistently support the prevailing hypothesis that pseudo bulges are disk components masquerading as bulges. Pseudo bulges were formed from stars born out of gas accumulated in the central regions of the galaxy (Kormendy & Kennicutt 2004; Sellwood 2014; Tonini et al. 2016; Izquierdo-Villalba et al. 2019). Since their formation resembles the assembly of galaxy disks, pseudo bulges manifest themselves as diffuse (low  $\langle \mu_e \rangle$ ), approximately exponential ( $n \approx 1$ ), and intrinsically flattened (broad distribution of  $\epsilon$ ) structures. Secular processes being inefficient and gradual, only relatively modest masses accumulate in the center (small  $B/T$ ). The products of secular processes are most frequently found in late-type spirals, as these systems have more fuel to feed central star formation and generally have experienced a more placid merger history. However, it is unclear which mechanisms

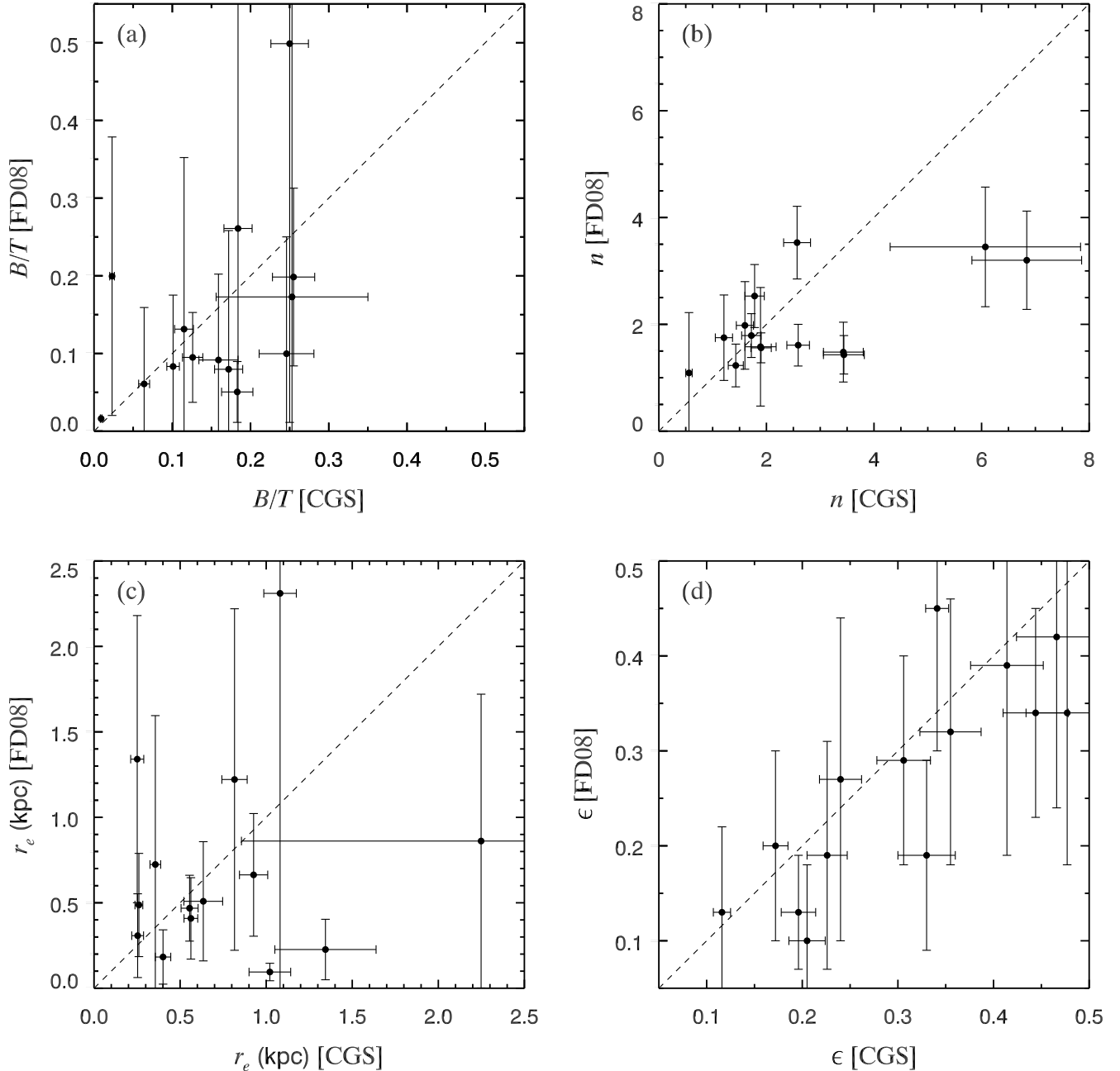


**Figure 15.** Comparison of CGS ( $R$  band) bulge parameters with those obtained by FD08 ( $V$  band) for the 14 galaxies in common between the two studies, for (a)  $B/T$ , (b)  $n$ , (c)  $r_e$ , and (d)  $\epsilon$ . Dashed lines are one-to-one relations.

are mainly responsible for driving gas inflow. Nonaxisymmetries such as bars, lenses/ovals, and spiral arms contribute to secular evolution, among them bars often thought to be the most effective. Intriguingly, the analysis in Section 3.7 shows no preference for barred galaxies to host pseudo bulges. We will revisit this issue in Section 4.3.2.

On the other hand, the broad distribution of  $B/T$  and  $n$  of classical bulges implicates a variable formation efficiency. Ellipticals and classical bulges can be made

viably through major mergers (Hopkins et al. 2009a,b, 2010; Brooks & Christensen 2016; Tonini et al. 2016; Rodriguez-Gomez et al. 2017). Violent relaxation of preexisting stars and central starbursts resulting from the rapid inflow of gas create bulges of high Sérsic indices and pressure-supported stellar orbits. The efficiency of bulge formation depends on the gas fraction of the merger, and the degree to which the merger remnant reacquires a stellar disk (Hopkins et al. 2009a,b, 2010). Minor mergers can also contribute to the formation or



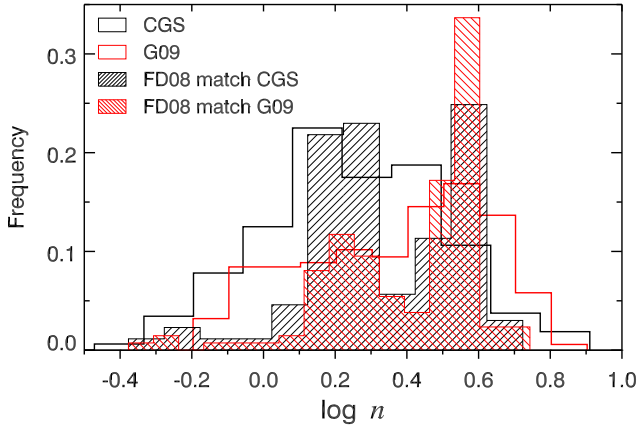


**Figure 16.** Comparison of bulge Sérsic index distributions for the sample of CGS (unfilled black histogram), G09 (unfilled red histogram), and FD08 (filled black and red histogram), after matching the relative number of classical to pseudo bulges. Bulges with  $\log n < -0.5$  in CGS are omitted.

growth of classical bulges, albeit in a less prominent (Aguerri et al. 2001; Eliche-Moral et al. 2006; Hopkins et al. 2010) and more complicated manner. Minor mergers can either contribute directly to the bulge or trigger disk instabilities and indirectly contribute to bulge growth in a secular manner. The density of the satellite is a determining factor: a dense satellite more likely survives to the center and contributes to the growth of a classical bulge, while a diffuse satellite can be tidally disrupted halfway (Aguerri et al. 2001; Eliche-Moral et al. 2006). More massive satellites, of course, lead to more dramatic effects.

Moreover, coalescence of giant clumps in high-redshift disks can form classical bulges (Noguchi 1999; Bournaud et al. 2007, 2009; Elmegreen et al. 2008; Bournaud 2016). The disks of gas-rich, vigorously star-forming, high-redshift galaxies fragment into massive clumps of stars and gas and exhibit irregular morphologies as a result of stellar feedback and gravitationally instability. The clumps in what are commonly refer to as clumpy or chain galaxies then migrate inward through dynamical friction and merge into a bulge. Although the physical processes are driven by disk instability, they are nothing like the secular evolution in  $z \approx 0$  disks, as the migration and coalescence of clumps operate on much shorter timescales (several hundreds of Myr; see Noguchi 1999 and Genzel et al. 2008). Clump coalescence, along with violent relaxation, creates highly concentrated, dispersion-supported, high- $[\alpha/\text{Fe}]$  ratio spheroids that resemble ellipticals, which, by definition, are classical bulges (Immel et al. 2004; Elmegreen et al. 2008). The accretion timescale, mass, and mass density of the galaxies can

produce a broad spectrum of bulge prominence, down to values as small as  $B/T \approx 0.1$  (Noguchi 1999; Bournaud et al. 2007). This seems to be consistent with the observed broad distribution of  $B/T$  for classical bulges (Figure 3). However, not all investigators agree that bulges originate from clumps. Oklopčić et al. (2017) used cosmological hydrodynamic simulations with a realistic stellar feedback treatment to show that clumps are short-lived and do not systematically migrate inward.

The broad outlines for the formation of classical and pseudo bulges seem more or less in order. The secular processes that build pseudo bulges at  $z \approx 0$  are inefficient and produce mostly weak bulges. The resulting disk component retains enough memory of its origin that it can be distinguished from classical bulges in various respects. Classical bulges form with variable efficiency through rapid processes involving violent relaxation and gaseous dissipation at an early epoch. Their structural parameters follow the scaling relations (e.g., Kormendy relation and fundamental plane) of ellipticals, and they are spheroids instead of flattened structures like pseudo bulges. The formation picture, however, still has some loose ends. Some studies maintain that mergers can make pseudo bulges (Wang et al. 2015; Eliche-Moral et al. 2018; Sauvaget et al. 2018), although the pseudo bulges may still be the products of secular processes of the rebuilt disks after the gas-rich mergers settle down. Inoue & Saitoh (2012) suggest that clump coalescence can lead to pseudo bulges, even if, overall, the ultimate fate of clumps is still controversial (Oklopčić et al. 2017). A quantitative comparison between our measurements with theoretical predictions would be highly desirable, but this lies beyond the scope of this paper. Previous studies have revealed possible inconsistencies. According to Weinzirl et al. (2009), semi-analytic  $\Lambda$ CDM models predict too many prominent bulges compared with observations. At the same time, other authors consider the pseudo bulges to be overabundant compared to cosmological predictions (Kormendy & Fisher 2008; Kormendy et al. 2010). It is also puzzling to see no signs of a classical bulge in massive disk galaxies such as NGC 4565 (Kormendy & Barentine 2010). The lower pseudo bulge fractions in early-type disks reported in this study perhaps helps alleviate the tension.

#### 4.3.2. The Driving Engines of Secular Evolution

In Section 3.7, we found that bars do not bear any obvious relation to pseudo bulges, not even in gas-rich galaxies. This is counterintuitive, as bars, the strongest nonaxisymmetric structure in the disk, are thought to

drive efficient gas inflow. Perhaps it indicates that non-axisymmetries other than bars, such as lenses/ovals and spiral arms, also participate in driving gas inflow. As these additional nonaxisymmetries are ubiquitous features in disk galaxies, the presence or absence of pseudo bulges does not have to rely on bars alone.

Still, because other nonaxisymmetries are weaker than bars, we need to understand why barred galaxies have pseudo bulges of comparable strength and frequency as unbarred galaxies (Figure 13). We caution that the observed  $B/T$  of pseudo bulges represents the accumulated growth of their prolonged history, and is not necessarily related to the present-day observable properties of the galaxy, such as its current gas fraction and presence of a bar. Today’s gas-poor galaxies may once have been gas-rich. At any rate, pseudo bulges are generically weak ( $B/T \lesssim 0.1$ ), and hence the host does not need to be extraordinarily gas-rich to provide the fuel. This may explain why the  $B/T$  of pseudo bulges does not depend on current gas fraction (Figure 13). Another outstanding issue pertains to whether bars are long-lived (Athanasoula et al. 2013) or not (Bournaud & Combes 2002). Central mass concentrations such as black holes and compact bulges weaken and even dissolve bars (Combes 1996; Shen & Sellwood 2004; Bournaud et al. 2005), but they can be regenerated from gas accretion (Combes 1996; Bournaud & Combes 2002; Block et al. 2002; Bournaud et al. 2005). Therefore, present-day unbarred galaxies may once have been barred, during which time their pseudo bulges were built. If so, we expect that at fixed  $B/T$  and gas fraction, the pseudo bulges of barred galaxies should have younger stellar populations. This hypothesis should be tested in the future. The evolutionary state of the bar may also matter. In gas-rich systems where bars have the best chance to make a difference between barred and unbarred galaxies, bars may have developed later and are weaker when mature (Athanasoula et al. 2013). Mature bars suffer from buckling instability and form boxy/peanut bulges, which reduce gas inflow to the very center (Fragkoudi et al. 2016). Bar-driven secular evolution itself may be self-regulated: the very growth of a pseudo bulge may weaken the bar and thereby curtail its own growth rate. This may weaken any systematic differences between barred and unbarred systems. Finally, external perturbations, such as ram-pressure striping, flybys, and minor mergers may also promote gas inflows (e.g., Moore et al. 1996, 1998, 1999; Bekki 1999; Bekki & Couch 2011; Kaviraj 2014; Poggianti et al. 2017). Such external effects would be incredibly difficult to disentangle from internal secular processes.

To summarize: despite the lack of clear observational evidence that bars directly relate to the pseudo bulge phenomenon, the above considerations prevent us from drawing any firm conclusions about their actual role.

## 5. SUMMARY

We use robustly measured structural parameters of a large, homogeneous sample of 320 lenticular and spiral galaxies to investigate the Kormendy ( $\langle\mu_e\rangle$  vs.  $r_e$ ) relation of their bulge components. The bulge parameters are derived from detailed 2D decomposition of high-quality  $R$ -band images drawn from CGS. We critically discuss the empirical classification of bulge types, reexamine the statistical properties of classical and pseudo bulges, and consider their physical implications.

Our principal results are as follows.

- Despite the ambiguities in classification of bulge types, we find that pseudo bulges selected as low- $\langle\mu_e\rangle$  outliers of the Kormendy relation established by elliptical galaxies generally show physical properties consistent with their presumed disk origin.
- The distribution of bulge Sérsic indices is not bimodal. We recommend abandoning the common practice of adopting  $n \approx 2$  to distinguish between classical and pseudo bulges.
- In line with Gadotti (2009) and Neumann et al. (2017), we recommend using the Kormendy relation as a promising alternative to using Sérsic index to classify bulges.
- Pseudo bulges have low Sérsic indices, most having  $n \lesssim 2$ , with the distribution peaking at  $n \approx 1$ , consistent with disk-like profiles. Most pseudo bulges are weak, comprising only  $B/T \lesssim 0.1$  of the total light.
- Classical bulges display a broad distribution in  $B/T$  and  $n$ , and are on average more prominent than pseudo bulges, despite their significant overlap in  $B/T$ .
- Pseudo bulges are intrinsically more flattened structures compared with classical bulges. The ellipticities of pseudo bulges are consistent with those of disks.
- Pseudo bulges reside most frequently in less massive, gas-rich late-type spirals.
- Contrary to naive expectations, barred galaxies do not host more pseudo bulges or more prominent pseudo bulges than unbarred galaxies.

The statistical properties of our sample reveal a number of quantitative differences compared to previous studies that can be understood in terms of our improved method of 2D image decomposition and different classification criteria applied. In qualitative agreement with previous studies, we suggest that pseudo bulges formed through internal secular processes in the large-scale disk, where nonaxisymmetries drive gas inflow and build up central overdensities through star formation. Their disky origin is still encoded in their low surface brightnesses, near-exponential radial profiles, and flat-

tened geometry. Classical bulges formed via violent processes akin to those in elliptical galaxies.

We thank the referee for constructive comments. This work was supported by the National Science Foundation of China (11721303, 11991052) and the National Key R&D Program of China (2016YFA0400702). H.G. thanks Jing Wang and Hassen Yesuf for useful discussions.

## APPENDIX

### A. *R*-BAND STRUCTURAL PARAMETERS OF CGS ELLIPTICALS

The CGS ellipticals provide the fiducial scaling relations for comparison with bulges. We performed single-Sérsic fits to derive their global structural parameters ( $n$ ,  $\mu_e$ , and  $r_e$ ) in the *R* band. Although Li et al. (2011) give access to non-parametric measurements of the structural parameters, we consider our parametric analysis necessary because we wish to avoid possible systematic biases due to measurement technique. Comparison of the two sets of measurements (Figure 17, top panels) reveals that that Sérsic fits indeed yield values of  $\mu_e$  and  $r_e$  that are systematically larger from the non-parametric ones. This is expected, as Sérsic fits integrate the flux to infinity, whereas non-parametric methods measure the flux only within the radius where the galaxy light fades into the noise. The tests of Trujillo et al. (2001) show that the differences between the two kinds of measurements depend on the Sérsic index and the size of the galaxy relative to the aperture applied to measure its flux: the larger the galaxy size and Sérsic index, the more significant the differences between the parametric and non-parametric measurements, as more light would be missed by the non-parametric methods. The bottom panels of Figure 17 confirm this trend. Galaxies with larger normalized  $r_e$  and larger  $n$  show larger offsets in the two structural parameters.

Although we choose Sérsic-based parameters for the ellipticals to facilitate a consistent comparison with the bulges, there are concerns about these measurements that need to be addressed. First, the measurements are model-dependent, as we already know that ellipticals can be better fit by multiple Sérsic components (Huang et al. 2013a). Second, we do not know the light distributions beyond the limiting surface brightness of the images, so it is dangerous to recklessly extrapolate to infinity. The three-component Sérsic fits of Huang et al. (2013a), which conform to the two-phase scenario for the origin of ellipticals (Huang et al. 2013b), in principle should describe more accurately the outermost component of the galaxy and therefore provide more reasonable extrapolation at large radii. Huang et al. (2016) presented three-component Sérsic fits of a subset of the CGS ellipticals in the *R* band. Figure 18 shows good agreement between the total magnitudes derived from our single-Sérsic fits and their three-Sérsic fits. Systematic bias is negligible (0.03 mag), and the rms scatter is 0.19 mag. This comparison assures us that the total light of the ellipticals obtained from single-Sérsic fits is reasonable, at least when compared with state-of-art parametric measurements.

We only have to deal with the extreme outliers. There are four galaxies (NGC 1172, 2865, 4936, and 4976) that exhibit offsets larger than 2 times the rms. We remeasure their  $\mu_e$ ,  $\langle\mu_e\rangle$ , and  $r_e$  using the curve-of-growth method, but using total magnitudes obtained from the three-Sérsic fits as input instead of the total magnitudes obtained from the non-parametric method. However, this method failed in the case of NGC 4936, for its  $r_e$  lies beyond the image boundary, so we apply no further corrections for it. We also correct for NGC 1439, because it appears as an outlier in the Kormendy relation. Correcting the structural parameters of these four galaxies has little effect on the scaling relation.

The best-fit models for the ellipticals are displayed in Figure 19, and their structural parameters are listed in Table 2.

**Fig. Set 19. Best-fit models of CGS ellipticals.**

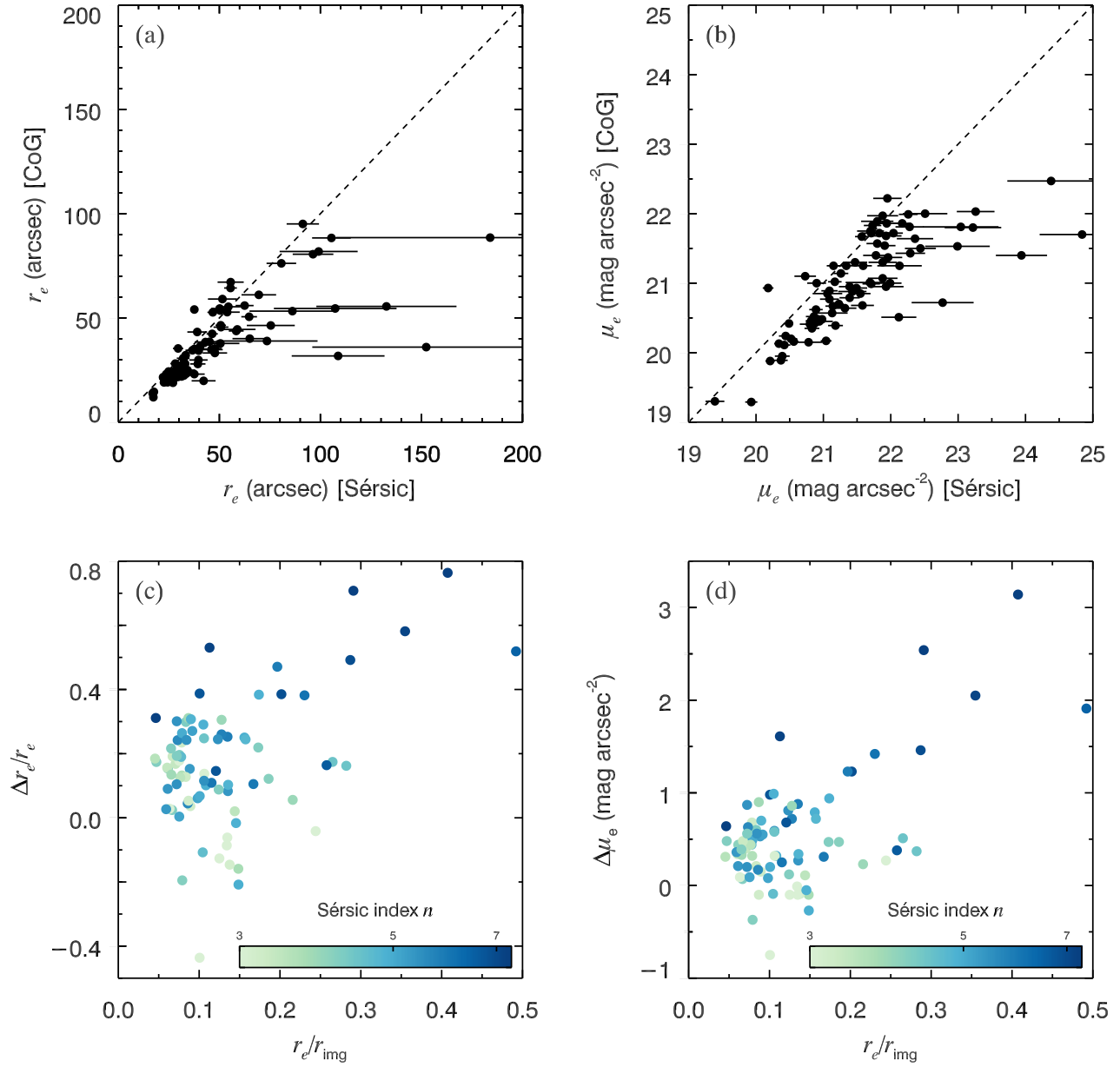


**Figure 17.** Comparison of Sérsic structural parameters (a)  $r_e$  and (b)  $\mu_e$  with non-parametric ones based on the curve-of-growth (CoG) analysis of the CGS ellipticals. Dependence of the differences in (c)  $r_e$  and (d)  $\mu_e$  on galaxy size normalized by the image size and on Sérsic index.

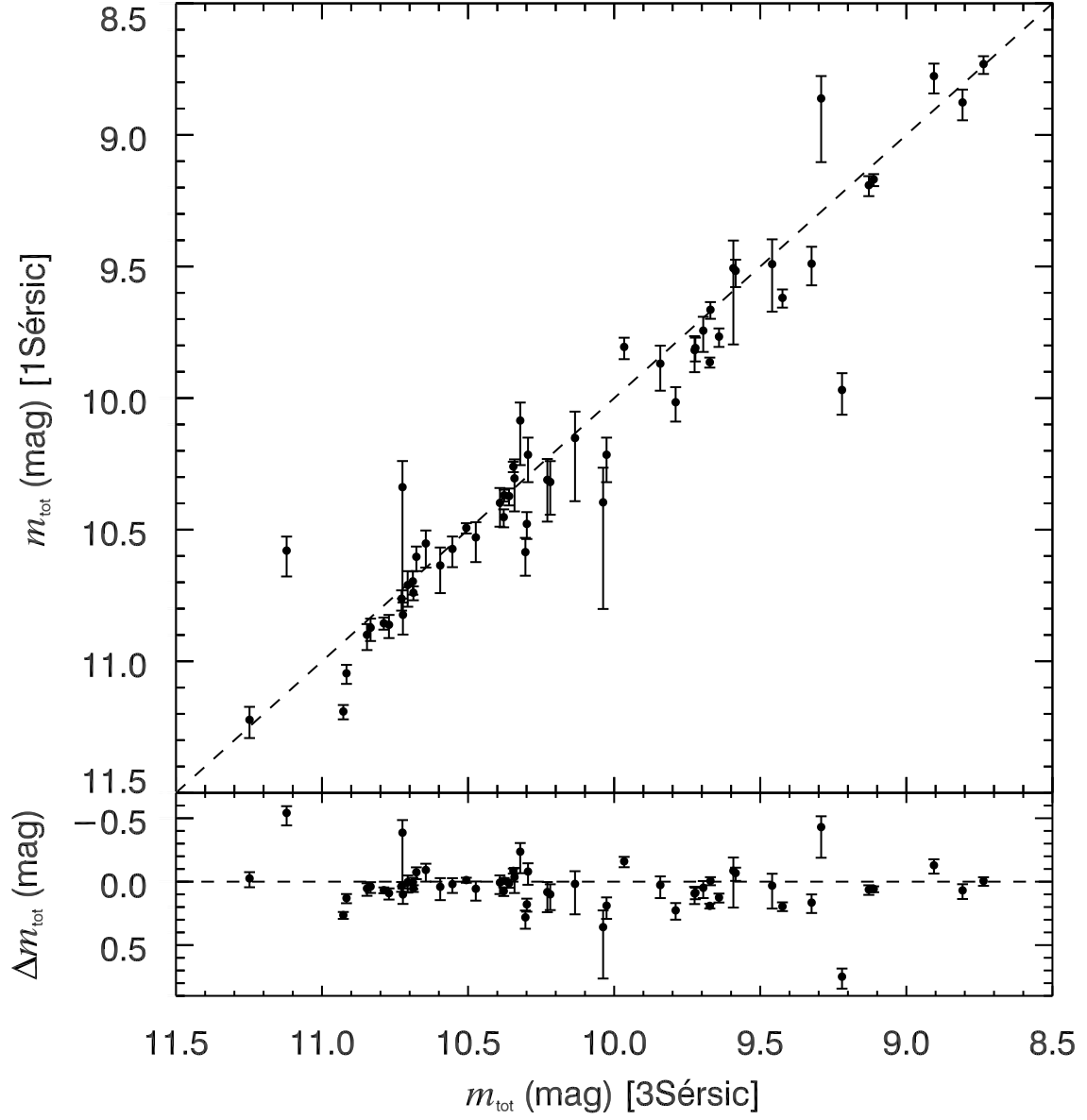


**Figure 18.** Comparison of total magnitudes of the CGS ellipticals obtained through single-Sérsic fits with those through three-Sérsic fits. There is no significant systematic bias ( $\langle \Delta m_{\text{tot}} \rangle = 0.03 \pm 0.19 \text{ mag}$ ).

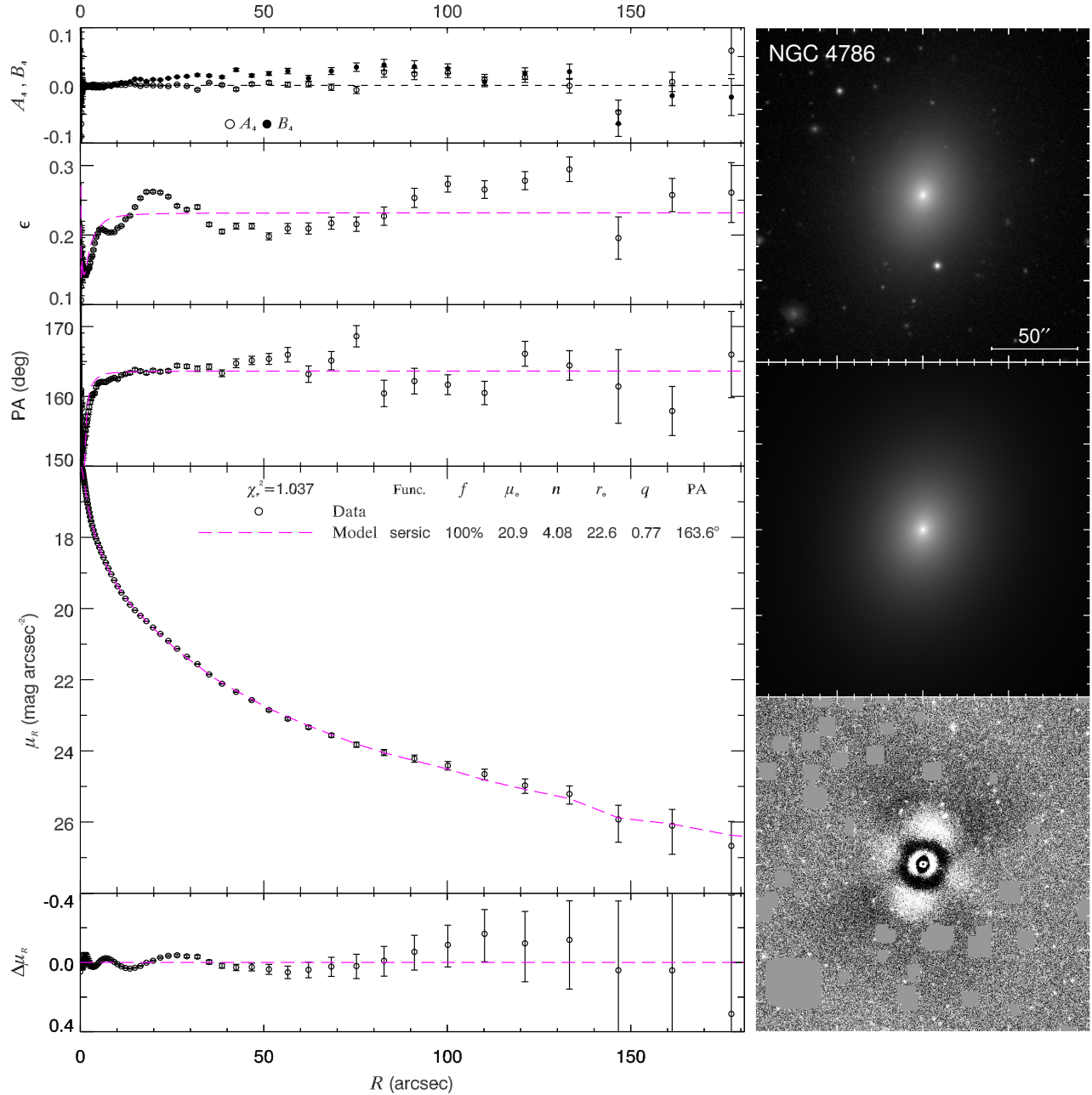


**Figure 19.** Best-fit model of NGC 4786. The left panels display the isophotal analysis of the 2D image fitting. From top to bottom, the panels show the radial profiles of the fourth harmonic deviations from an ellipse ( $A_4$  and  $B_4$ ), ellipticity ( $\epsilon$ ), position angle (PA),  $R$ -band surface brightness ( $\mu_R$ ), and fitting residuals ( $\Delta\mu_R$ ). Profiles of the data and model are encoded consistently with different symbols, line styles, and colors, as explained in the legends. The text to the right of the legends gives detailed information on each component; from left to right, the columns describe the radial profile functions (Sérsic), the light fractions, the effective surface brightness  $\mu_e$ , the Sérsic index  $n$ , the effective radius  $r_e$ , the axis ratio  $q$ , and the PA. Note that the surface brightness profile of the model is generated by fixing the geometric parameters to those of the data surface brightness profile. The right panels display, from top to bottom, the grayscale  $R$ -band image, the best-fit model image, and the residual image. The images are shown using the same logarithmic stretch for the data and model image, and histogram equalization stretch for the residual image. All images are cropped to have the same size of  $1.5D_{25}$ , with  $D_{25}$  the isophotal galaxy diameter at  $\mu_B = 25 \text{ mag arcsec}^{-2}$ , and are centered on the galaxy centroid, with north up and east to the left. (The complete figure set for 83 elliptical galaxies is available in the online journal.)

**Table 2.** Best-fit Parameters of the CGS Ellipticals

| Name         | $\langle\mu_e\rangle$<br>(mag arcsec <sup>-2</sup> ) | $n$         | $r_e$<br>(kpc) | $\epsilon$    |
|--------------|------------------------------------------------------|-------------|----------------|---------------|
| (1)          | (2)                                                  | (3)         | (4)            | (5)           |
| ESO 185-G054 | 20.76 ± 0.20                                         | 4.94 ± 0.26 | 18.71 ± 2.46   | 0.269 ± 0.000 |
| IC 1459      | 19.31 ± 0.09                                         | 5.19 ± 0.12 | 6.61 ± 0.34    | 0.261 ± 0.000 |
| IC 1633      | 21.56 ± 0.25                                         | 6.69 ± 0.34 | 35.50 ± 5.58   | 0.167 ± 0.000 |
| IC 2311      | 19.15 ± 0.19                                         | 5.18 ± 0.29 | 2.90 ± 0.34    | 0.043 ± 0.000 |
| IC 2597      | 20.35 ± 0.12                                         | 4.97 ± 0.17 | 7.04 ± 0.54    | 0.284 ± 0.000 |
| IC 3370      | 19.54 ± 0.08                                         | 3.92 ± 0.15 | 4.53 ± 0.23    | 0.164 ± 0.000 |
| IC 3896      | 19.97 ± 0.29                                         | 5.49 ± 0.42 | 7.03 ± 1.31    | 0.208 ± 0.002 |
| IC 4296      | 20.28 ± 0.19                                         | 4.97 ± 0.23 | 13.37 ± 1.56   | 0.084 ± 0.001 |
| IC 4742      | 20.05 ± 0.29                                         | 3.89 ± 0.51 | 8.28 ± 1.71    | 0.192 ± 0.002 |
| IC 4765      | 22.53 ± 0.59                                         | 6.05 ± 0.66 | 52.04 ± 21.53  | 0.362 ± 0.001 |
| IC 4797      | 18.71 ± 0.09                                         | 4.52 ± 0.16 | 3.37 ± 0.20    | 0.399 ± 0.001 |
| IC 4889      | 19.02 ± 0.06                                         | 4.07 ± 0.09 | 3.56 ± 0.13    | 0.336 ± 0.000 |
| IC 5328      | 19.62 ± 0.12                                         | 4.26 ± 0.19 | 4.93 ± 0.36    | 0.288 ± 0.002 |
| NGC 596      | 19.59 ± 0.06                                         | 5.14 ± 0.10 | 3.30 ± 0.12    | 0.126 ± 0.001 |
| NGC 636      | 20.22 ± 0.23                                         | 6.42 ± 0.40 | 4.63 ± 0.63    | 0.119 ± 0.000 |
| NGC 720      | 18.85 ± 0.07                                         | 3.22 ± 0.09 | 4.36 ± 0.20    | 0.420 ± 0.000 |
| NGC 1052     | 18.88 ± 0.06                                         | 3.97 ± 0.10 | 2.96 ± 0.10    | 0.295 ± 0.000 |
| NGC 1172     | 21.05 ± 0.86                                         | ...         | 7.03 ± 3.41    | 0.207 ± 0.002 |
| NGC 1199     | 19.79 ± 0.13                                         | 4.61 ± 0.20 | 4.84 ± 0.37    | 0.249 ± 0.001 |
| NGC 1209     | 18.92 ± 0.05                                         | 4.58 ± 0.10 | 3.85 ± 0.13    | 0.524 ± 0.000 |
| NGC 1339     | 18.87 ± 0.08                                         | 4.58 ± 0.16 | 1.78 ± 0.09    | 0.284 ± 0.000 |
| NGC 1340     | 19.13 ± 0.07                                         | 3.59 ± 0.12 | 3.51 ± 0.17    | 0.354 ± 0.000 |
| NGC 1374     | 19.48 ± 0.05                                         | 4.62 ± 0.09 | 2.66 ± 0.09    | 0.097 ± 0.000 |
| NGC 1379     | 19.56 ± 0.05                                         | 3.12 ± 0.08 | 2.47 ± 0.08    | 0.019 ± 0.000 |
| NGC 1395     | 19.65 ± 0.09                                         | 4.33 ± 0.12 | 5.89 ± 0.33    | 0.163 ± 0.001 |
| NGC 1399     | 19.64 ± 0.10                                         | 4.58 ± 0.12 | 5.93 ± 0.35    | 0.093 ± 0.001 |
| NGC 1404     | 18.06 ± 0.11                                         | 3.31 ± 0.18 | 2.14 ± 0.15    | 0.136 ± 0.001 |
| NGC 1407     | 20.17 ± 0.14                                         | 4.42 ± 0.17 | 9.32 ± 0.85    | 0.046 ± 0.000 |
| NGC 1426     | 19.87 ± 0.18                                         | 5.09 ± 0.33 | 3.72 ± 0.42    | 0.350 ± 0.000 |
| NGC 1427     | 20.11 ± 0.11                                         | 5.45 ± 0.18 | 4.84 ± 0.35    | 0.299 ± 0.000 |
| NGC 1439     | 21.02 ± 0.41                                         | ...         | 6.95 ± 1.58    | 0.090 ± 0.000 |
| NGC 1453     | 20.07 ± 0.20                                         | 5.63 ± 0.29 | 10.81 ± 1.35   | 0.163 ± 0.001 |
| NGC 1521     | 20.32 ± 0.18                                         | 5.25 ± 0.26 | 10.91 ± 1.22   | 0.300 ± 0.001 |
| NGC 1549     | 19.64 ± 0.10                                         | 4.96 ± 0.14 | 4.64 ± 0.29    | 0.103 ± 0.000 |
| NGC 1600     | 20.32 ± 0.20                                         | 3.75 ± 0.27 | 12.39 ± 1.72   | 0.329 ± 0.002 |
| NGC 1700     | 19.11 ± 0.17                                         | 5.33 ± 0.28 | 5.31 ± 0.55    | 0.287 ± 0.000 |
| NGC 2305     | 19.70 ± 0.14                                         | 4.82 ± 0.19 | 4.98 ± 0.43    | 0.251 ± 0.000 |

*Table 2 continued*

Table 2 (continued)

| Name     | $\langle \mu_e \rangle$<br>(mag arcsec $^{-2}$ ) | $n$         | $r_e$<br>(kpc) | $\epsilon$    |
|----------|--------------------------------------------------|-------------|----------------|---------------|
| (1)      | (2)                                              | (3)         | (4)            | (5)           |
| NGC 2325 | 20.18 ± 0.11                                     | 2.95 ± 0.12 | 5.53 ± 0.41    | 0.364 ± 0.000 |
| NGC 2434 | 19.74 ± 0.18                                     | 4.71 ± 0.27 | 4.21 ± 0.48    | 0.089 ± 0.001 |
| NGC 2663 | 20.05 ± 0.29                                     | 4.73 ± 0.35 | 13.22 ± 2.57   | 0.332 ± 0.001 |
| NGC 2865 | 18.44 ± 0.17                                     | ...         | 2.28 ± 0.27    | 0.250 ± 0.000 |
| NGC 2986 | 20.44 ± 0.11                                     | 5.57 ± 0.17 | 10.70 ± 0.76   | 0.151 ± 0.000 |
| NGC 3078 | 19.23 ± 0.17                                     | 5.00 ± 0.27 | 4.93 ± 0.51    | 0.241 ± 0.000 |
| NGC 3087 | 19.64 ± 0.16                                     | 5.33 ± 0.24 | 5.95 ± 0.59    | 0.149 ± 0.000 |
| NGC 3091 | 20.24 ± 0.19                                     | 5.24 ± 0.27 | 10.81 ± 1.32   | 0.286 ± 0.001 |
| NGC 3136 | 20.68 ± 0.43                                     | 6.73 ± 0.58 | 12.43 ± 3.52   | 0.264 ± 0.001 |
| NGC 3250 | 19.26 ± 0.12                                     | 3.85 ± 0.17 | 6.30 ± 0.47    | 0.256 ± 0.001 |
| NGC 3258 | 20.16 ± 0.20                                     | 4.80 ± 0.26 | 7.74 ± 0.97    | 0.127 ± 0.001 |
| NGC 3268 | 21.22 ± 0.50                                     | 5.51 ± 0.61 | 14.45 ± 4.92   | 0.203 ± 0.000 |
| NGC 3557 | 19.54 ± 0.10                                     | 4.58 ± 0.13 | 8.11 ± 0.49    | 0.242 ± 0.000 |
| NGC 3585 | 19.98 ± 0.17                                     | 6.24 ± 0.25 | 8.22 ± 0.86    | 0.445 ± 0.001 |
| NGC 3923 | 20.20 ± 0.14                                     | 4.71 ± 0.17 | 10.69 ± 0.97   | 0.343 ± 0.001 |
| NGC 3962 | 19.96 ± 0.11                                     | 4.91 ± 0.16 | 7.49 ± 0.54    | 0.202 ± 0.000 |
| NGC 4696 | 20.72 ± 0.12                                     | 2.99 ± 0.13 | 16.65 ± 1.46   | 0.219 ± 0.000 |
| NGC 4709 | 21.32 ± 0.38                                     | 5.70 ± 0.47 | 15.42 ± 3.80   | 0.155 ± 0.000 |
| NGC 4742 | 18.06 ± 0.08                                     | 7.99 ± 0.17 | 1.26 ± 0.06    | 0.400 ± 0.000 |
| NGC 4760 | 20.73 ± 0.19                                     | 4.42 ± 0.25 | 12.68 ± 1.61   | 0.155 ± 0.001 |
| NGC 4767 | 19.23 ± 0.10                                     | 4.17 ± 0.16 | 5.03 ± 0.33    | 0.423 ± 0.001 |
| NGC 4786 | 19.37 ± 0.10                                     | 4.08 ± 0.16 | 6.87 ± 0.44    | 0.232 ± 0.000 |
| NGC 4936 | 20.21 ± 0.17                                     | 4.14 ± 0.22 | 8.13 ± 0.94    | 0.170 ± 0.001 |
| NGC 4976 | 19.02 ± 0.37                                     | ...         | 3.25 ± 0.82    | 0.320 ± 0.001 |
| NGC 5011 | 20.17 ± 0.15                                     | 5.06 ± 0.22 | 7.23 ± 0.68    | 0.158 ± 0.000 |
| NGC 5018 | 18.52 ± 0.06                                     | 4.39 ± 0.10 | 4.79 ± 0.18    | 0.297 ± 0.000 |
| NGC 5044 | 20.27 ± 0.12                                     | 3.12 ± 0.14 | 8.23 ± 0.69    | 0.060 ± 0.000 |
| NGC 5061 | 19.50 ± 0.15                                     | 6.48 ± 0.25 | 5.70 ± 0.53    | 0.099 ± 0.001 |
| NGC 5077 | 19.14 ± 0.14                                     | 4.56 ± 0.21 | 5.45 ± 0.47    | 0.302 ± 0.001 |
| NGC 5328 | 19.80 ± 0.14                                     | 5.23 ± 0.21 | 7.94 ± 0.66    | 0.313 ± 0.000 |
| NGC 5419 | 20.63 ± 0.18                                     | 4.55 ± 0.23 | 15.78 ± 1.95   | 0.210 ± 0.000 |
| NGC 5791 | 19.21 ± 0.09                                     | 3.98 ± 0.15 | 4.43 ± 0.26    | 0.425 ± 0.000 |
| NGC 5796 | 19.55 ± 0.14                                     | 5.06 ± 0.22 | 5.23 ± 0.45    | 0.131 ± 0.000 |
| NGC 5812 | 19.32 ± 0.10                                     | 5.24 ± 0.17 | 3.63 ± 0.23    | 0.044 ± 0.000 |
| NGC 5898 | 19.27 ± 0.20                                     | 4.59 ± 0.28 | 3.88 ± 0.49    | 0.019 ± 0.001 |
| NGC 5903 | 20.48 ± 0.24                                     | 4.87 ± 0.31 | 9.05 ± 1.39    | 0.232 ± 0.000 |
| NGC 6851 | 18.89 ± 0.07                                     | 4.20 ± 0.14 | 2.74 ± 0.13    | 0.266 ± 0.000 |
| NGC 6868 | 20.04 ± 0.18                                     | 4.94 ± 0.23 | 8.08 ± 0.90    | 0.186 ± 0.000 |
| NGC 6876 | 20.19 ± 0.08                                     | 3.05 ± 0.10 | 9.05 ± 0.52    | 0.136 ± 0.000 |

Table 2 continued



Table 2 (continued)

| Name     | $\langle \mu_e \rangle$<br>(mag arcsec <sup>-2</sup> ) | $n$         | $r_e$<br>(kpc) | $\epsilon$    |
|----------|--------------------------------------------------------|-------------|----------------|---------------|
| (1)      | (2)                                                    | (3)         | (4)            | (5)           |
| NGC 6909 | 20.05 ± 0.14                                           | 4.37 ± 0.25 | 5.33 ± 0.49    | 0.442 ± 0.000 |
| NGC 6958 | 19.18 ± 0.07                                           | 5.17 ± 0.11 | 3.55 ± 0.16    | 0.144 ± 0.000 |
| NGC 7029 | 19.41 ± 0.07                                           | 5.23 ± 0.11 | 4.75 ± 0.19    | 0.364 ± 0.000 |
| NGC 7145 | 20.42 ± 0.15                                           | 4.94 ± 0.21 | 4.41 ± 0.42    | 0.036 ± 0.000 |
| NGC 7196 | 19.28 ± 0.13                                           | 4.58 ± 0.21 | 5.41 ± 0.42    | 0.217 ± 0.000 |
| NGC 7507 | 18.80 ± 0.09                                           | 4.99 ± 0.13 | 4.11 ± 0.22    | 0.038 ± 0.000 |
| NGC 7796 | 20.03 ± 0.13                                           | 4.91 ± 0.19 | 8.13 ± 0.66    | 0.153 ± 0.000 |

NOTE—Col. (1): Galaxy name. Cols. (2)–(5): Average effective surface brightness, Sérsic index, effective radius, and ellipticity. The parameters are measured in the  $R$  band and have been corrected for Galactic extinction.

## REFERENCES

- Aguerri, J. A. L., Balcells, M., & Peletier, R. F. 2001, *A&A*, 367, 428
- Allen, P. D., Driver, S. P., Graham, A. W., et al. 2006, *MNRAS*, 371, 2
- Athanassoula, E. 2005, *MNRAS*, 358, 1477
- Athanassoula, E., Machado, R. E. G., & Rodionov, S. A. 2013, *MNRAS*, 429, 1949
- Balcells, M., Graham, A. W., Domínguez-Palmero, L., & Peletier, R. F. 2003, *ApJL*, 582, L79
- Bekki, K. 1999, *ApJL*, 510, L15
- Bekki, K., & Couch, W. J. 2011, *MNRAS*, 415, 1783
- Bender, R. 1987, *MitAG*, 70, 226
- Bender, R. 1988, *A&A*, 193, L7
- Bender, R., Burstein, D., & Faber, S. M. 1992, *ApJ*, 399, 462
- Bertin, G., Ciotti, L., & Del Principe, M. 2002, *A&A*, 386, 149
- Binggeli, B. 1994, in *ESO/OHP Workshop on Dwarf Galaxies*, ed. G. Meylan & P. Prugniel (Garching: ESO), 13
- Binney, J., & Tremaine, S. 2008, *Galactic Dynamics: Second Edition* (Princeton, NJ: Princeton Univ. Press)
- Block, D. L., Bournaud, F., Combes, F., Puerari, I., & Buta, R. 2002, *A&A*, 394, L35
- Borriello, A., Salucci, P., & Danese, L. 2003, *MNRAS*, 341, 1109
- Bournaud, F. 2016, in *Galactic Bulges*, ed. E. Laurikainen, R. Peletier, & D. Gadotti (New York: Springer), 355
- Bournaud, F., & Combes, F. 2002, *A&A*, 392, 83
- Bournaud, F., Combes, F., & Semelin, B. 2005, *MNRAS*, 364, L18
- Bournaud, F., Elmegreen, B. G., & Elmegreen, D. M. 2007, *ApJ*, 670, 237
- Bournaud, F., Elmegreen, B. G., & Martig, M. 2009, *ApJL*, 707, L1
- Brooks, A., & Christensen, C. 2016, in *Galactic Bulges*, ed. E. Laurikainen, R. Peletier, & D. Gadotti (New York: Springer), 317
- Busarello, G., Capaccioli, M., Capozziello, S., Longo, G., & Puddu, E. 1997, *A&A*, 320, 415
- Cappellari, M., Bacon, R., Bureau, M., et al. 2006, *MNRAS*, 366, 1126
- Cappellari, M., McDermid, R. M., Alatalo, K., et al. 2012, *Nature*, 484, 485
- Cappellari, M., Scott, N., Alatalo, K., et al. 2013a, *MNRAS*, 432, 1709
- Cappellari, M., McDermid, R. M., Alatalo, K., et al. 2013b, *MNRAS*, 432, 1862
- Carollo, C. M. 1999, *ApJ*, 523, 566
- Carollo, C. M., Stiavelli, M., de Zeeuw, P. T., & Mack, J. 1997, *AJ*, 114, 2366
- Carollo, C. M., Stiavelli, M., Seigar, M., de Zeeuw, P. T., & Dejonghe, H. 2002, *AJ*, 123, 159
- Chown, R., Li, C., Athanassoula, E., et al. 2019, *MNRAS*, 484, 5192
- Ciotti, L., Lanzoni, B., & Renzini, A. 1996, *MNRAS*, 282, 1

- Cleveland, W. S., & Devlin, S. J. 1988, *Journal of the American Statistical Association*, 83, 596
- Combes, F. 1996, in *ASP Conf. Ser. 91, IAU Coll. 157: Barred Galaxies*, ed. R. Buta, D. A. Crocker, & B. G. Elmegreen (San Francisco, CA: ASP), 286
- Combes, F., Debbasch, F., Friedli, D., & Pfenniger, D. 1990, *A&A*, 233, 82
- Combes, F., & Sanders, R. H. 1981, *A&A*, 96, 164
- Costantin, L., Corsini, E. M., Méndez-Abreu, J., et al. 2018, *MNRAS*, 481, 3623
- Costantin, L., Méndez-Abreu, J., Corsini, E. M., et al. 2017, *A&A*, 601, A84
- Davies, R. L., Efstathiou, G., Fall, S. M., Illingworth, G., & Schechter, P. L. 1983, *ApJ*, 266, 41
- de Jong, R. S. 1996, *A&A*, 313, 45
- de Lorenzo-Cáceres, A., Méndez-Abreu, J., Thorne, B., & Costantin, L. 2019, *MNRAS*, 484, 665
- de Vaucouleurs, G. 1948, *AnAp*, 11, 247
- Djorgovski, S. 1987, in *IAU Symp. 127, Structure and Dynamics of Elliptical Galaxies*, ed. P. T. de Zeeuw (Dordrecht: Reidel), 79
- Djorgovski, S., & Davis, M. 1987, *ApJ*, 313, 59
- Djorgovski, S., de Carvalho, R., & Han, M.-S. 1988, in *ASP Conf. Ser. 4, The Extragalactic Distance Scale*, ed. S. van den Bergh & C. J. Pritchet (San Francisco, CA: ASP), 329
- D'Onofrio, M., Cariddi, S., Chiosi, C., Chiosi, E., & Marziani, P. 2017, *ApJ*, 838, 163
- D'Onofrio, M., Fasano, G., Moretti, A., et al. 2013, *MNRAS*, 435, 45
- Dressler, A., Lynden-Bell, D., Burstein, D., et al. 1987, *ApJ*, 313, 42
- Eliche-Moral, M. C., Balcels, M., Aguerri, J. A. L., & González-García, A. C. 2006, *A&A*, 457, 91
- Eliche-Moral, M. C., Rodríguez-Pérez, C., Borlaff, A., Querejeta, M., & Tapia, T. 2018, *A&A*, 617, A113
- Elmegreen, B. G., Bournaud, F., & Elmegreen, D. M. 2008, *ApJ*, 688, 67
- Emsellem, E., Cappellari, M., Krajnović, D., et al. 2011, *MNRAS*, 414, 888
- Erwin, P., Saglia, R. P., Fabricius, M., et al. 2015, *MNRAS*, 446, 4039
- Faber, S. M. 1977, in *Evolution of Galaxies and Stellar Populations*, ed. B. M. Tinsley & R. B. Larson (New Haven, CT: Yale Univ. Obs.), 157
- Faber, S. M., Dressler, A., Davies, R. L., Burstein, D., & Lynden-Bell, D. 1987, in *Nearly Normal Galaxies. From the Planck Time to the Present*, ed. S. M. Faber (New York: Springer), 175
- Faber, S. M., & Jackson, R. E. 1976, *ApJ*, 204, 668
- Faber, S. M., Tremaine, S., Ajhar, E. A., et al. 1997, *AJ*, 114, 1771
- Fisher, D. B., & Drory, N. 2008, *AJ*, 136, 773
- Fisher, D. B., & Drory, N. 2010, *ApJ*, 716, 942
- Fisher, D. B., & Drory, N. 2016, in *Galactic Bulges*, ed. E. Laurikainen, R. Peletier, & D. Gadotti (New York: Springer), 41
- Fisher, D. B., Drory, N., & Fabricius, M. H. 2009, *ApJ*, 697, 630
- Fragkoudi, F., Athanassoula, E., & Bosma, A. 2016, *MNRAS*, 462, L41
- Fukugita, M., Shimasaku, K., & Ichikawa, T. 1995, *PASP*, 107, 945
- Gadotti, D. A. 2008, *MNRAS*, 384, 420
- Gadotti, D. A. 2009, *MNRAS*, 393, 1531
- Gallagher, J. S., Goad, J. W., & Mould, J. 1982, *ApJ*, 263, 101
- Gao, H., & Ho, L. C. 2017, *ApJ*, 845, 114
- Gao, H., Ho, L. C., Barth, A. J., & Li, Z.-Y. 2018, *ApJ*, 862, 100
- Gao, H., Ho, L. C., Barth, A. J., & Li, Z.-Y. 2019, *ApJS*, 244, 34
- Genzel, R., Burkert, A., Bouché, N., et al. 2008, *ApJ*, 687, 59
- Gott, III, J. R. 1977, *ARA&A*, 15, 235
- Grosbøl, P., Patsis, P. A., & Pompei, E. 2004, *A&A*, 423, 849
- Ho, L. C., Li, Z.-Y., Barth, A. J., Seigar, M. S., & Peng, C. Y. 2011, *ApJS*, 197, 21
- Hopkins, P. F., Cox, T. J., Younger, J. D., & Hernquist, L. 2009a, *ApJ*, 691, 1168
- Hopkins, P. F., Somerville, R. S., Cox, T. J., et al. 2009b, *MNRAS*, 397, 802
- Hopkins, P. F., Bundy, K., Croton, D., et al. 2010, *ApJ*, 715, 202
- Huang, S., Ho, L. C., Peng, C. Y., Li, Z.-Y., & Barth, A. J. 2013a, *ApJ*, 766, 47
- Huang, S., Ho, L. C., Peng, C. Y., Li, Z.-Y., & Barth, A. J. 2013b, *ApJL*, 768, L28
- Huang, S., Ho, L. C., Peng, C. Y., Li, Z.-Y., & Barth, A. J. 2016, *ApJ*, 821, 114
- Illingworth, G. 1977, *ApJL*, 218, L43
- Immeli, A., Samland, M., Gerhard, O., & Westera, P. 2004, *A&A*, 413, 547
- Inoue, S., & Saitoh, T. R. 2012, *MNRAS*, 422, 1902
- Izquierdo-Villalba, D., Bonoli, S., Spinoso, D., et al. 2019, *MNRAS*, 488, 609
- Kaviraj, S. 2014, *MNRAS*, 440, 2944
- Kent, S. M. 1985, *ApJS*, 59, 115
- Kim, M., & Ho, L. C. 2019, *ApJ*, 876, 35

- Kim, M., Ho, L. C., Peng, C. Y., Barth, A. J., & Im, M. 2017, *ApJS*, 232, 21
- Kodaira, K., Watanabe, M., & Okamura, S. 1986, *ApJS*, 62, 703
- Kormendy, J. 1977, *ApJ*, 218, 333
- Kormendy, J. 1981, in *The Structure and Evolution of Normal Galaxies*, ed. S. M. Fall & D. Lynden-Bell (Cambridge: Cambridge Univ. Press), 85
- Kormendy, J. 1982a, *ApJ*, 257, 75
- Kormendy, J. 1982b, in *Twelfth Advanced Course of the Swiss Society of Astronomy and Astrophysics, Morphology and Dynamics of Galaxies*, ed. L. Martinet & M. Mayor (Sauverny: Geneva Obs.), 113
- Kormendy, J. 1985, *ApJ*, 295, 73
- Kormendy, J. 1987, in *Nearly Normal Galaxies. From the Planck Time to the Present*, ed. S. M. Faber (New York: Springer), 163
- Kormendy, J. 1993, in *IAU Symp. 153, Galactic Bulges*, ed. H. Dejonghe & H. J. Habing (Dordrecht: Kluwer), 209
- Kormendy, J. 2013, in *Secular Evolution of Galaxies*, ed. J. Falcón-Barroso & J. H. Knapen (Cambridge: Cambridge Univ. Press), 1
- Kormendy, J. 2016, in *Galactic Bulges*, ed. E. Laurikainen, R. Peletier, & D. Gadotti (New York: Springer), 431
- Kormendy, J., & Barentine, J. C. 2010, *ApJL*, 715, L176
- Kormendy, J., & Djorgovski, S. 1989, *ARA&A*, 27, 235
- Kormendy, J., Drory, N., Bender, R., & Cornell, M. E. 2010, *ApJ*, 723, 54
- Kormendy, J., & Fisher, D. B. 2008, in *ASP Conf. Ser. 396, Formation and Evolution of Galaxy Disks*, ed. J. G. Funes & E. M. Corsini (San Francisco, CA: ASP), 297
- Kormendy, J., Fisher, D. B., Cornell, M. E., & Bender, R. 2009, *ApJS*, 182, 216
- Kormendy, J., & Ho, L. C. 2013, *ARA&A*, 51, 511
- Kormendy, J., & Illingworth, G. 1982, *ApJ*, 256, 460
- Kormendy, J., & Illingworth, G. 1983, *ApJ*, 265, 632
- Kormendy, J., & Kennicutt, Jr., R. C. 2004, *ARA&A*, 42, 603
- Kormendy, J., Byun, Y., Ajhar, E. A., et al. 1996, in *IAU Symp. 171, New Light on Galaxy Evolution*, ed. R. Bender & R. L. Davies (Dordrecht: Kluwer), 105
- Kroupa, P. 2001, *MNRAS*, 322, 231
- Läscher, R., Greene, J. E., Seth, A., et al. 2016, *ApJ*, 825, 3
- Lauer, T. R. 1985, *ApJ*, 292, 104
- Lauer, T. R., Ajhar, E. A., Byun, Y.-I., et al. 1995, *AJ*, 110, 2622
- Lauer, T. R., Faber, S. M., Gebhardt, K., et al. 2005, *AJ*, 129, 2138
- Lauer, T. R., Gebhardt, K., Faber, S. M., et al. 2007, *ApJ*, 664, 226
- Laurikainen, E., Salo, H., Buta, R., & Knapen, J. H. 2007, *MNRAS*, 381, 401
- Laurikainen, E., Salo, H., Buta, R., Knapen, J. H., & Comerón, S. 2010, *MNRAS*, 405, 1089
- Li, Z.-Y., Ho, L. C., & Barth, A. J. 2017, *ApJ*, 845, 87
- Li, Z.-Y., Ho, L. C., Barth, A. J., & Peng, C. Y. 2011, *ApJS*, 197, 22
- Lin, L., Li, C., He, Y., Xiao, T., & Wang, E. 2017, *ApJ*, 838, 105
- Lynden-Bell, D., Faber, S. M., Burstein, D., et al. 1988, *ApJ*, 326, 19
- Méndez-Abreu, J., Aguerri, J. A. L., Corsini, E. M., & Simonneau, E. 2008, *A&A*, 478, 353
- Méndez-Abreu, J., Simonneau, E., Aguerri, J. A. L., & Corsini, E. M. 2010, *A&A*, 521, A71
- Méndez-Abreu, J., Ruiz-Lara, T., Sánchez-Menguiano, L., et al. 2017, *A&A*, 598, A32
- Méndez-Abreu, J., Aguerri, J. A. L., Falcón-Barroso, J., et al. 2018, *MNRAS*, 474, 1307
- Moore, B., Katz, N., Lake, G., Dressler, A., & Oemler, A. 1996, *Nature*, 379, 613
- Moore, B., Lake, G., & Katz, N. 1998, *ApJ*, 495, 139
- Moore, B., Lake, G., Quinn, T., & Stadel, J. 1999, *MNRAS*, 304, 465
- Neumann, J., Wisotzki, L., Choudhury, O. S., et al. 2017, *A&A*, 604, A30
- Nieto, J.-L., Bender, R., & Surma, P. 1991, *A&A*, 244, L37
- Noguchi, M. 1999, *ApJ*, 514, 77
- Oklopčić, A., Hopkins, P. F., Feldmann, R., et al. 2017, *MNRAS*, 465, 952
- Pahre, M. A., de Carvalho, R. R., & Djorgovski, S. G. 1998, *AJ*, 116, 1606
- Paturel, G., Petit, C., Prugniel, P., et al. 2003, *A&A*, 412, 45
- Peng, C. Y., Ho, L. C., Impey, C. D., & Rix, H.-W. 2002, *AJ*, 124, 266
- Peng, C. Y., Ho, L. C., Impey, C. D., & Rix, H.-W. 2010, *AJ*, 139, 2097
- Pfenniger, D. 1984, *A&A*, 134, 373
- Pfenniger, D. 1985, *A&A*, 150, 112
- Pfenniger, D., & Norman, C. 1990, *ApJ*, 363, 391
- Poggianti, B. M., Jaffé, Y. L., Moretti, A., et al. 2017, *Nature*, 548, 304
- Renzini, A. 1999, in *The Formation of Galactic Bulges*, ed. C. M. Carollo, H. C. Ferguson, & R. F. G. Wyse (Cambridge: Cambridge Univ. Press), 9
- Renzini, A., & Ciotti, L. 1993, *ApJL*, 416, L49
- Roberts, M. S., & Haynes, M. P. 1994, *ARA&A*, 32, 115
- Rodriguez-Gomez, V., Sales, L. V., Genel, S., et al. 2017, *MNRAS*, 467, 3083

- Sandage, A., Freeman, K. C., & Stokes, N. R. 1970, *ApJ*, 160, 831
- Sauvaget, T., Hammer, F., Puech, M., et al. 2018, *MNRAS*, 473, 2521
- Sellwood, J. A. 2014, *RvMP*, 86, 1
- Sellwood, J. A., & Wilkinson, A. 1993, *RPPh*, 56, 173
- Sérsic, J. L. 1968, *Atlas de Galaxias Australes* (Córdoba: Obs. Astron., Univ. Nac. Córdoba)
- Shen, J., & Sellwood, J. A. 2004, *ApJ*, 604, 614
- Simien, F., & de Vaucouleurs, G. 1986, *ApJ*, 302, 564
- Tabor, M., Merrifield, M., Aragón-Salamanca, A., et al. 2017, *MNRAS*, 466, 2024
- Tonini, C., Mutch, S. J., Croton, D. J., & Wyithe, J. S. B. 2016, *MNRAS*, 459, 4109
- Toomre, A. 1977, in *Evolution of Galaxies and Stellar Populations*, ed. B. M. Tinsley & R. B. Larson (New Haven, CT: Yale Univ. Obs.), 401
- Treu, T., Ellis, R. S., Liao, T. X., & van Dokkum, P. G. 2005, *ApJL*, 622, L5
- Trujillo, I., Graham, A. W., & Caon, N. 2001, *MNRAS*, 326, 869
- van den Bergh, S. 1976, *ApJ*, 203, 764
- Wang, J., Hammer, F., Puech, M., Yang, Y., & Flores, H. 2015, *MNRAS*, 452, 3551
- Wang, J., Kauffmann, G., Overzier, R., et al. 2012, *MNRAS*, 423, 3486
- Weinzirl, T., Jogee, S., Khochfar, S., Burkert, A., & Kormendy, J. 2009, *ApJ*, 696, 411
- Wyse, R. F. G., Gilmore, G., & Franx, M. 1997, *ARA&A*, 35, 637
- Zhang, H., & Zaritsky, D. 2016, *MNRAS*, 455, 1364
- Zhao, D., Ho, L. C., Zhao, Y., Shanguan, J., & Kim, M. 2019, *ApJ*, 877, 52